Theory of Electro-Optic Sensors – A Tutorial

By

Richard L. Garcia

A MASTER OF ENGINEERING REPORT

Submitted to the College of Engineering at
Texas Tech University in
Partial Fulfillment of
The Requirements for the
Degree of

MASTER OF ENGINEERING

Approved

_____
Dr. J. Borrelli

_____
Dr. A. Ertas

_____
Dr. T. Maxwell

_____
Dr. M. Tanik

October 21, 2006

ACKNOWLEDGEMENTS

This masters degree program has been very challenging and rewarding. Dr. Atila Ertas, Dr. Timothy Maxwell, Dr. Murat Tanik, and the excellent group of professors were truly superb. I learned a lot from my classmates as well, especially Jon Ilseng, Justa Tevino, and Mark Midoux with whom I worked on several group projects. I hope I did at least my fair share. I want to thank Mike Marquis for his instruction of Raytheon's "Fundamentals of Thermal Imaging Systems" course and his review of this report. The course was very valuable to my learning process and to this project. I would like to thank my many "bosses" over this past year that gave me the support and encouragement to complete the course, including Amy Brunson, Robert Gonzalez, and Bill Shieldes. I would like to especially thank Brent Wells for the confidence he showed in me by selecting me for this program. Brent has been a valuable mentor for me over the last 11 years at Raytheon. Finally, I could not have completed this program without the love and support from my family: my son Ricky, my daughter Melinda, my grandson Ethan, and foremost my wife Lupe. She has been incredible with her understanding, encouragement, and consideration, as I had to give up much of our time together to complete this program. They, along with my mother Sue, father Jack, sister Stacey, and step-father Jim, give me the inspiration and drive to continue to challenge myself and my career.

TABLE OF CONTENTS

ACKNOWLEDGEMENTS **1**

DISCLAIMER **5**

ABSTRACT **6**

LIST OF FIGURES **7**

LIST OF TABLES **8**

CHAPTER I
INTRODUCTION **9**

1.1 Review of Key References 10
1.2 The Electromagnetic Spectrum 12
1.3 The Ideal Optical Sensor 13
1.4 Fundamentals of Infrared Imagining 14

CHAPTER II
BRIEF HISTORY OF ELECTRO-OPTIC SENSORS **16**

2.1 Initial Discoveries 16
2.2 Early Systems – From Theory to Application 16
2.3 FLIRs and Real Time Imagers 17
2.4 Detector Technologies – GEN I 18
2.5 Passivation – GEN II 19
2.6 Multi- and Hyperspectral Arrays – GEN III 20

CHAPTER III
PRINCIPLES OF INFRARED SYSTEMS **22**

3.1 Radiation Theory 22
3.1.1 Blackbody 22
3.1.2 Planck's Law 22
3.1.3 Stefan-Boltzmann Law 24
3.1.4 Radiometric Terms 26
3.1.5 Lambert's Cosine Law 26
3.1.6 Kirchoff's Law 28
3.2 Atmospheric Transmission 29
3.2.1 Absorption 31
3.2.2 Scattering 31
3.2.3 Mie and Rayleigh Scattering 32
3.2.4 Beer's Law 33
3.2.5 Transmission Analysis 34
3.3 Optics 34
3.4 Optical Performance 41
3.5 Infrared Detectors 43
3.5.1 Figures of Merit 44
3.5.1.1 Responsivity 44
3.5.1.2 Noise Equivalent Power 45
3.5.1.3 Detectivity 46

3.5.1.4 Quantum Efficiency 46
3.5.2 Detector Noise 48
3.5.2.1 1/*f* Noise 49
3.5.2.2 Johnson Noise 49
3.5.2.3 Generation-Recombination Noise 50
3.5.2.4 Summation of Noise Sources 50
3.5.3 Background Limited Performance 51
3.5.4 Detector Performance 51
CHAPTER IV
INFRARED SENSOR DESIGN 57
4.1 System Architecture 57
4.2 Component Materials 58
4.2.1 Optical Materials 58
4.2.1.1 Refractive Index 59
4.2.1.2 Strength and Hardness 59
4.2.1.3 Absorption 60
4.2.1.4 Thermal Expansion 61
4.2.1.5 Summary 62
4.2.2 Detectors 62
4.2.2.1 Mercury Cadmium Telluride (HgCdTe) 63
4.2.2.2 Platinum Silicide (PtSi) 65
4.2.2.3 Indium Antimonide (InSb) 66
4.2.2.4 Extrinsic Silicon (Si) Detectors 67
4.2.2.5 Lead Sulfide (PbS) and Lead Selenide (PbSe) 68
4.2.2.6 Summary 69
4.2.3 Readout Electronics 70
4.2.3.1 MOSFET Primer 71
4.2.3.2 ROIC Performance Drivers 72
4.2.3.3 Signal Processing 73
4.2.3.4 Data Multiplexers 74
4.2.3.5 Output Video Amplifiers 75
4.2.4 Cooling Systems 75
4.2.4.1 Design Fundamentals 76
4.2.4.2 Low Temperature Heat Sink 76
4.2.5 Displays 78
4.2.5.1 Cathode-Ray Tubes 78
4.2.5.2 Plasma Panels 79
4.2.5.3 Electroluminescent Panels 79
4.2.5.4 Liquid Crystals 79
4.2.5.5 Light Emitting Diodes 80
4.2.5.6 Projection Displays 80
4.3 System of Systems 81
CHAPTER V
MODELING OF INFRARED SYSTEMS 82
5.1 Noise Equivalent Temperature Difference 82
5.2 Minimum Detectable Temperature Difference 83

5.3 Detection Analysis 84
5.4 IR System Analysis 87
CHAPTER VI
CURRENT CAPABILITES..... 91
6.1 AN/ASQ-228 Advanced Targeting Forward Looking Infrared (ATFLIR) 91
6.2 AN/AAS-52 Multi-Spectral Targeting System (MTS) 92
6.3 AN/PAS-13B Thermal Weapon Sight 93
6.4 AN/AAQ-28(V) LITENING AT 94
6.5 NICMOS –Hubble Space Telescope 95
CHAPTER VII
SUMMARY 96
REFERENCES..... 97

DISCLAIMER

The opinions expressed in this report are strictly those of the author and are not necessarily those of Raytheon, Texas Tech University, nor any U.S. Government agency.

ABSTRACT

The objective of this report is to provide a very brief introduction to the theory of electro-optic systems, more specifically infrared (IR) sensors. Engineers and engineering students can use this report to gain a high level understanding of how IR sensors work. It is also intended for those just beginning work in this technology or those specializing in a specific technology desired an understanding of the larger system. The report describes various IR systems and a brief history of how they were developed, including key enabling technologies. The underlying scientific and engineering principles of IR sensors are presented. Also included is the basic design of the system, common materials used in the components, and approaches to assessing performance. MATLAB is used to present an example analysis of system performance.

LIST OF FIGURES

FIGURE 1. REMOTE THERMAL SIGHT DISPLAY 9
FIGURE 2. ELECTROMAGNETIC SPECTRUM. 12
FIGURE 3. SPECTRAL RADIANT EMITTANCE 24
FIGURE 4. RADIANT EMITTANCE 25
FIGURE 5. RADIATION EXCHANGE 27
FIGURE 6. RADIANCE 28
FIGURE 7. ATMOSPHERIC WINDOWS 30
FIGURE 8. REFRACTION AND REFLECTION 35
FIGURE 9. SIMPLE LENS 36
FIGURE 10. FOCAL LENGTH 37
FIGURE 11. GENERALIZED OPTICAL SYSTEM 38
FIGURE 12. OBJECT AND IMAGE RELATIONSHIP 39
FIGURE 13. TWO-COMPONENT SYSTEM 40
FIGURE 14. QUANTUM EFFICIENCY 47
FIGURE 15. NOISE POWER SPECTRAL DENSITY CURVE 48
FIGURE 16. BLACKBODY DETECTOR TESTING CONFIGURATION 52
FIGURE 17. BASIC IR SYSTEM DESIGN 57
FIGURE 18. SILICON AND GERMANIUM LENSES 62
FIGURE 19. DETECTOR MATERIALS FOR IR APPLICATIONS 63
FIGURE 20. PBS FOCAL PLANE ARRAY 70
FIGURE 21. ASIC READOUT ELECTRONICS BOARD 71
FIGURE 22. STERLING CRYOCOOLER 78
FIGURE 23. TOTAL INTEGRATION TRANSMISSION VERSUS RANGE 85
FIGURE 24. FRAME RATE 88
FIGURE 25. DETECTIVITY 88
FIGURE 26. SCAN EFFICIENCY 89
FIGURE 27. OPTICS TRANSMISSION 90
FIGURE 28. ATFLIR 92
FIGURE 29. MTS 92
FIGURE 30. THERMAL WEAPON SYSTEM 93
FIGURE 31. LITENING AT 94
FIGURE 32. NICMOS 95

LIST OF TABLES

TABLE 1. SCATTERING COEFFICIENTS 33
TABLE 2. MASS EXTINCTION COEFFICIENTS 33
TABLE 3. SAMPLE DATA FOR IR PHOTOCONDUCTOR 52
TABLE 4. REFRACTIVE INDICIES 59
TABLE 5. STRENGTH AND HARDNESS 60
TABLE 6. ABSORPTION COEFFICIENT AND DISPERSION INDEX 61
TABLE 7. THERMAL EXPANSION COEFFICIENTS 61
TABLE 8. TYPICAL PERFORMANCE SPECIFICATION FOR AN LWIR PV HGCDTE ARRAY 64
TABLE 9. TYPICAL PERFORMANCE OF HYBRID PTSI ARRAYS AT 77 K 65
TABLE 10. TYPICAL PERFORMANCE OF INSB ASTRONOMY ARRYS 66
TABLE 11. COMMON IMPURITY LEVELS USED IN EXTRINSIC SI IR DETECTORS 67
TABLE 12. TYPICAL PERFORMANCE OF SI:GA ASTRONOMY ARRAYS 68
TABLE 13. TYPICAL PERFORMANCE OF PBSE LINEAR ARRAY WITH CMOS MULTIPLEXED READOUT 69
TABLE 14. DETECTOR MATERIAL PERFORMANCE PARAMETERS 69
TABLE 15. KEY READOUT REQUIREMENTS AND SYSTEMS PERFORMANCE AND INTERFACE ISSUES 72
TABLE 16. TYPES OF CRYOGENIC REFRIGERATORS 77
TABLE 17. TOW SYSTEM PARAMETERS 84

CHAPTER I
INTRODUCTION

Shock and Awe, Own the night, Smart Bombs, Collateral damage, Orion Nebula, Near Earth Asteroid, Situational Awareness. These are terms that have become part of our lexicon over last few decades. The common denominator is the advancement of electro-optic systems. While speaking at the 2002 DARPA Systems and Technology Symposium, General Richard Myers, then Chairman of the Joint Chiefs of Staff, stated that there are three technologies that have changed the nature of modern warfare: Night vision, precision strike, and global positioning system [Silver, 2005(1)]. Two of these technologies are enabled by electro-optic systems. Night vision systems allow US soldiers to have a significant advantage over the enemy during operations at night and during limited visibility. Figure1 [Defense Update, 2006] is the Remote Thermal Sight display on the M1 Abrams Tank, which allows the tank commander to engage targets with his .50-caliber machine gun while buttoned-up, day or night. Electro-optic infrared sensors in missiles have increased lethality; enabled precision strike of enemy targets, and significantly reduced collateral damage. We have seen the videos of missiles and bombs, launched from miles away fly through the window of the targeted building.

Figure 1. Remote Thermal Sight Display

Networks of infrared sensors on aircraft and Unmanned Arial Vehicles (UAV) for surveillance and reconnaissance have increased the commander's knowledge of the battlefield, the situational awareness of both friendly and enemy forces. So much knowledge, that commanders are reaching

information overload, requiring development of improved data and image processing, and sensor fusion to make sense of it all. The increases in situational awareness and precision strike capabilities, coupled with other technologies such as stealth, global positioning systems, and advanced communications, have resulted in new war fighting techniques. The "Rapid Dominance" [Ullman, 1996] doctrine emerged in the mid 1990s, following Desert Storm and attempted in Operation Iraqi Freedom in 2003. The core characteristic and capabilities of Rapid Dominance, or Shock and Awe, are *knowledge, rapidity, control of environment, and brilliance*. Each of these capabilities is enabled through applications of electro-optic sensors.

Infrared sensors aboard the Hubble space telescope have beamed back images more spectacular than anyone imagined (except the chief engineer). We have seen further and with more clarity than ever before, helping us to understand the beginning of our universe and inspiring a different sense of Shock and Awe. Scientists are making new discoveries almost daily.

The objective of this report is to provide a very brief introduction to the theory of electro-optic systems, more specifically infrared (IR) sensors. This project is my attempt to begin the learning process into this technology. Engineers and engineering students can use this report to gain a high level understanding of how IR sensors work, the underlying scientific and engineering principles, basic design of the system, common materials used in the components, and approaches to assessing performance. To reiterate, I am not the expert in this area. I am on the road of discovery and ask the reader to share my journey. And, hopefully you can save a little time in figuring out where to start (after looking up *electro-optic* in the dictionary). This report is a conglomeration of the references cited. If you, the reader, are the expert, I welcome you comments, criticism, and coaching.

1.1 Review of Key References

There are two key references used in this report. But the overall structure, especially Chapter III, is attributed to the "Fundamentals of Thermal Imaging Systems" course taught at Raytheon by Mr. Mike

Marquis. This was an excellent course taught by a very knowledgeable systems engineer. Some of the course material is reproduced in this report, or where possible, the original source is referenced.

Thermal Imaging Systems [Lloyd, 1975] is an excellent text. It is widely quoted in related literature. Though dated, it contains a very good analysis of the scientific theories underlying IR sensors. The laws, theorems, and derivations that contribute to the understanding and application to this field are presented.

The Infrared and Electro-Optical Systems Handbook is an eight-volume set which is the best guide for any engineer involved in IR/EO technologies. Two volumes used extensively in this report are Volume 3 Electro-Optical Components [Rogatto, 1993] for much of Chapter IV, and Volume 4 Electro-Optical Systems Design, Analysis, and Testing [Dudzik, 1993] from which the example in Chapter V was taken.

Infrared Technology – Applications to Electro-Optics, Photonic Devices, and Sensors [Jha, 2000] is also an excellent text containing EO theory, but mostly containing EO applications as the title suggests. It includes EO, IR, and lasers. It is a very good guide for detector technologies.

Optical Radiation Detectors [Dereniak, 1984] is an excellent text for detectors. It comprehensively covers several types of detectors, including photovoltaic detectors and photoconductors. It is becoming somewhat dated with more recent advances, but still provides the basis for additional research. Use the text for the theory, then research periodicals for current technology.

SPIE - The International Society for Optical Engineering (originally, Society of Photo-Optical Instrumentation Engineers), is an excellent repository of journals, publications, and proceedings, publishing the latest advancements in EO technologies.

Opto-Electronics Review is an international journal that includes scientific papers concerning the EO material, systems, and signal processing.

1.2 The Electromagnetic Spectrum

An electro-optic sensor operates by modifying the optical properties of a material by an electric field. This can be a change in absorption or a change in the refractive index. The energy in a light wave is relative to its wavelength. In visible light, violet has the most energy and thus the shortest wavelength. Red has the least energy and the longest wavelength. The Infrared (IR) spectrum is next to the visible light spectrum with longer wavelengths. The electromagnetic spectrum is shown in Figure 2 [NASA, 2001].

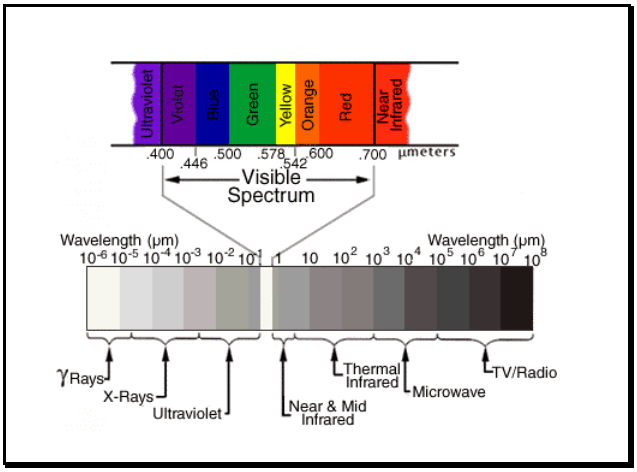

Figure 2. Electromagnetic Spectrum.

A basic television changes the visible light spectrum into an electronic image. An IR sensor works by capturing the infrared light in the form of photons reflected by or emitted from an object. A *photon* is the elementary particle responsible for electromagnetic phenomena. It mediates electromagnetic interactions and is the fundamental constituent of all forms of electromagnetic radiation, that is, light. The photon has zero rest mass and, in empty space, travels at a constant speed *c*; in the presence of matter, it can be slowed or even absorbed, transferring energy and momentum proportional to its frequency [Wikipedia, 2006]. A power source accelerates the photon image into a phosphorus screen to produce an image within the visible light spectrum for viewing. Night Vision Devices (NDVs) magnify the ambient light produced by the moon or stars to augment the reflected IR energy. Each of these systems is

considered an electro-optic sensor, each detecting different energy signals of different wavelengths. This report will concentrate primarily on IR sensor technologies.

There are three categories of IR light. Short Wave IR (SWIR) has wavelengths of 0.7 to 1.3 microns. Medium Wave IR (MWIR) wavelengths range from 1.3 to about 3 microns. Long Wave IR (LWIR), or thermal-IR, has wavelengths of 3 to over 30 microns. Thermal IR is emitted by an object while SWIR and LWIR is reflected from the object.

A thermal imager detects variations in the heat emitted by an object and its surroundings. These variations are assembled by various means to create a picture for the observer. The conditions that would normally obscure normal human vision, such as dust, fog, smoke, and clouds, are minimized. Heat sources such as a human body or engine exhaust can be detected at much greater ranges and with much greater clarity than with the naked eye. Night vision systems detect wavelengths up to 1.0 to 1.5 microns, which is slightly higher than what the human eye can detect.

1.3 The Ideal Optical Sensor

Consider the perfection at which the human eye produces visible images. There are three factors that contribute to the functional optimization of the eye as a sensor. First, the eye's response to the spectral range of 0.4 to 0.7 microns coincides with the sun's peak spectral output. Nearly 38 percent of the sun's radiant energy is concentrated in this band. Conversely, only 0.08 percent of the sun's energy is found within the 8 to 14 micron band. Terrestrial materials tend to have very good reflective properties in the 0.4 to 0.7 micron band. Second, the retinal detectors of the eye have low noise at the quantum energy levels in this band, making the eye an ideal quantum noise limited devise. Third, the response of the retinal detectors to the photons emitted at body temperature is negligible, so that this long wave thermal energy does not mask the response to the desired wavelengths. This capability allows the eye to effectively perform its functions, which are to detect reflectivity differences in objects illuminated in the objective radiation, discriminate patterns in these reflectivity responses, and to associate these patterns with abstractions derived from previous visual and other sensory experiences. [Rogatto, 1993].

Images in the visible spectrum are produced primarily by reflection and reflectivity differences. Thermal images, on the other hand, are produced mostly by self-emission and emissivity differences. Therefore, in thermal imaging we are interested in thermally self-generated energy patterns, resulting in detectable temperature differences. In a given scene, the temperature, reflectivity, and emissivity taken together at a given point can be represented as an effective temperature at that point. The variations in the effective temperature of a scene tend to correspond to the details in the visible scene. Thus, a thermal imaging system can provide a visible analog of the visual scene, and effectively transfer information from one spectral band to another. Like the eye, an effective IR system must collect, spectrally filter, and focus infrared radiation from a scene onto an optically scanned multi-element detector array. Additionally, unlike the eye however, the IR system must covert the collected radiation into the visible spectrum for observation by the human operator.

1.4 Fundamentals of Infrared Imagining

IR sensor systems involve the integration of several engineering disciplines. These disciplines include:

- Radiation theory and target signatures
- Atmospheric transmission of thermal radiation
- Optical design
- Detector and detector cooler operation
- Electronic and digital signal processing
- Video displays
- Human search processes and visual perception

The thermal imaging process can be described as a sequence of events. For each event, one or more of the disciplines listed above must be utilized to analyze the event, and the response of the system in order to achieve the desired or required effectiveness. These simple steps, taken together as a whole,

illustrate the complexity of modern IR systems [Rogatto, 1993] and emphasize the need for a systems engineering approach to design. Consider a military application:

Event 1: The target of interest exhibits an effective temperature difference from its background due to energy exchange with the environment, self-heating, emissivity differences, or reflective sources. Event 2: The atmosphere intervening between the target and the IR system attenuates and blurs the target system. Event 3: An operator uses means of pointing the limited field of view to search for targets using a search pattern and cues. Event 4: The IR system uses its properties of thermal sensitivity, image sharpness, spectral response, dynamic range, contrast rendition, and magnification to produce a visual facsimile of the thermal scene. Event 5: The observer uses his training, experience, and image interpretation skills to detect, recognize, and identify targets to the best of his ability under the workload and ambient conditions to which he is subjected.

Each of these processes will be discussed in further detail in the ensuing chapters. We can also describe this process as *The Life of a Photon*. It is emitted or reflected from an object. It then travels through space being absorbed, reflected, or attenuated. If absorbed, its journey is complete. If reflected, refracted, or attenuated, it continues it's travels, changing some of its characteristics. As it reaches an EO sensor, it is again reflected, refracted, absorbed, or attenuated through the lenses and mirrors of the senor optics until it is reaches the senor detector. There it is excited and transformed into electrical energy. The electrical energy is amplified, conditioned, and processed, then turned into a digital signal. The digital signal is processed again as it displayed. Here it once again becomes a photon, within the visible spectrum, and is absorbed by the eye of the observer. Quite a journey!

CHAPTER II
BRIEF HISTORY OF ELECTRO-OPTIC SENSORS

2.1 Initial Discoveries

The British astronomer, William Hershel is credited with the discovery of infrared radiation in the early nineteenth century. He used a prism to refract the light from the sun. Beyond the red visible spectrum, he detected the radiation using sensitive thermometers to observe an increase in temperature. The temperature, he discovered, increased higher further from the red light indicating a detectable energy source beyond visible light. Hershel's work evolved into the field of infrared spectroscopy. It would take more than 30 years for further development in this field, until more sensitive measuring equipment evolved. New detectors such as the radiation thermocouple and the diffraction grating spectrometer led the way for progress in both basic and applied research in the field. Throughout the nineteenth and early twentieth centuries, experimentation, research and studies in theory were the primary concern. It is during this period that we see the fundamental theories and laws of thermal radiation formulated. The studies of spectral and temperature dependence of thermal radiation led to the validation of Planck's quantum theory, the Stefan-Boltzmann distribution law, and Wien's displacement law. Heinrich Herz's experimental studies of the propagation of thermal radiation through empty space provided the verification of Maxwell's classical theory of electromagnetic radiation [Jha, 2000]. The first thermal imaging system was a somewhat insensitive non-scanning devise from the 1930s called the Evaporagraph. This early system was limited in contrast, sensitivity, and response time.

2.2 Early Systems – From Theory to Application

In the 1940s and during World War II, two other technologies emerged. The first was analogous to television systems, with discrete detectors and mechanically scanning capability. Other developments included an infrared vidicon or other non-scanning devices [Lloyd, 1975]. It was also during this period that the original night vision systems were created for the US Army. These devices used active infrared projection called IR Illuminator. A beam of near-IR light, invisible to the human eye, was projected to

the object and reflected back to the lens. This technology was very similar to the normal flashlight [Works, 2006]. The original scanning thermal imagers were called thermographs, with single detector element, two dimensional, slow framing scanners that recorded the image on film and were therefore not real-time devices. The Army built the first thermograph using a 16-inch searchlight reflector, a dual axis scanner, and a bolometer detector. The Army continued rapid development of thermographs through 1960. Up to the late 1950s, electrical signal frequency bandwidths were limited to a few hundred Hertz because poor detector response above this range gave low image signal-to-noise ratios. The first fast framing sensors were made possible by the development of cooled short-time-constant indium antimonide (InSb) and mercury doped germanium (Ge:Hg) photo detectors [Lloyd, 1975].

2.3 FLIRs and Real Time Imagers

The first real-time infrared sensor was an outgrowth of downward looking strip mapper technology. Strip mappers are essentially thermographs with the vertical scan motion generated by the aircraft motion relative to the ground, developed and used by the Army and the Air Force for reconnaissance. It was this aircraft mounted, real-time, downward and *forward looking infrared* sensor that gave way to the term FLIR, now used generically for most infrared sensors. In 1956, the University of Chicago built the first operating long wave FLIR with support from the Air Force. This modified strip mapper added a nodding elevation mirror to the counter-rotating wedge scanner so that the single detector element traced out a two-dimensional raster pattern. However, during this period following the Korean War, further development was not pursued without a pressing military need. In 1960, the Perkin-Elmer Corporation built the next real-time long wave FLIR. Built for the Army, this ground based devise was called the Prism Scanner because it used two rotating refractive prisms to generate a spiral scan for the single element InSb detector. It had a 5^{o} circular field with a 1 milliradian detector subtense, a frame rate of 0.2 frames per second, a thermal sensitivity of $1^{o}C$, and a long persistence phosphor CRT display. The Prism Scanner launched the continued development of ground-based sensors for the Army and civilian applications. This technology persisted for several years, nearly a decade, with improved compactness

and growing civilian applications [Lloyd, 1975]. It was during this period of the early 1960s that NVDs moved from active IR to passive IR, no longer projecting light. This generation saw the use of light intensifiers, but applied to ambient moon or starlight. These devices were referred to as "Starlight Scopes" in the Army [Works, 2006].

2.4 Detector Technologies – GEN I

Two independent programs resurrected the airborne FLIR concept in the early 1960s by the Air Force and Texas Instruments Inc., and by the Navy and Hughes Aircraft Company. Prototypes were completed and tested in 1965, and were so successful that they spawned an amazing proliferation of airborne FLIRs and applications, continuing through the mid 1970s [Lloyd, 1975]. In 1997, these two companies were merged with Raytheon Company and later formed the Space and Airborne Systems business area, today a leader in airborne electro-optic technologies. Also in the mid 1970s, advances in image intensifiers led to the next generation of NVDs for use in extremely low light conditions. The microchannel plate increased the sensitivity of the image intensifier tube. The microchannel plate increases the number of electrons as opposed to accelerating the electrons as in earlier generations. This advancement significantly decreased distortion and resulted in a much brighter, sharper image [Works, 2006]. Soldiers used this technology in NVDs through the 1980s and into Desert Storm.

The key enabling technology for detector devices that led to the proliferation of FLIR systems in the early and mid-1960s came in 1958. Lawson, Nielson, Putley and Young [Lawson, 1959] first synthesized Mercury Cadmium Telluride (HgCdTe) crystals in England at the Royal Radar Establishment. The evolution in the processes for growth of HgCdTe led to the development of three generations of detector devises and IR system technology. Over the last 40 years other materials have been introduced but have not matched the properties of HgCdTe. These key properties include an adjustable bandgap from 0.7 to 25 um, direct bandgap with high absorption coefficient, moderate dielectric constant and index of refraction, moderate thermal coefficient of expansion, and the availability of wide bandgap lattice-matched substrates for epitaxial growth. Epitaxy involves the growth of crystals

of one material on the crystal face of another or the same material. Epitaxy forms a thin film whose material lattice structure and orientation or lattice symmetry is identical to that of the substrate on which it is deposited. In the late 1960s and early 1970s, led tin telluride (PbSnTe), was also pursued. However, PbSnTe has a high dielectric constant compared to HgCdTe and a large temperature coefficient of expansion mismatch with silicon (Si), the main substrate material [Norton, 2002].

The first generation of HgCdTe detector devises was linear arrays of photoconductors. These devises emerged following the development of reproducible bulk growth techniques and anodic-oxide surface passivation. Passivation is the process of making a material "passive" in relation to another material prior to using the materials together. The Army Common Module utilized these photoconductors on a family of arrays, accounting for most of the production of tens of thousands of arrays used in sights and missile seekers. NASA and NOAA also employ photoconductors in a wide variety of applications of earth satellites and monitoring systems [Norton, 2002].

2.5 Passivation – GEN II

The second generation of HgCdTe devices is two-dimensional array of photodiodes, or photovoltaic devices, which was first demonstrated in the mid 1970s. The key technology needed to make photovoltaic devices possible was surface passivation. Anodic oxide was adequate for photoconductors, but the resulting surfaces were heavily accumulated with fixed positive charge. Silicon oxide was employed for passivation of HgCdTe in the early 1980s based upon low-temperature deposition using photochemical reaction. However, the surface properties could not be maintained when heated in a vacuum for extended periods of time, which is required for good vacuum packaging integrity. The oxides were also subject to surface charge buildup when operated in a space-radiation environment. With the advent of CdTe passivation in 1987, HgCdTe photodiodes could finally be reliably passivated, and showed little effect from the radiation found in space after vacuum packaging heating cycles. This development made possible the full-scale production of the second-generation devices. Scanning second-generation sensors improve both sensitivity and spatial resolution through the use of more detector

elements in both the scan and cross-scan directions. Scanning arrays have increased pixel counts significantly over first-generation arrays. Photovoltaic arrays of 240 X 4, 288 X 4, and 480 X 4 have replaced the 60, 120, and 180 element arrays limited by first generation photoconductors. Both computer memory chips and infrared focal planes rely on the progression of silicon integrated circuit processing technology because silicon readouts have paced the development of large focal planes. Large focal planes designed for astronomy have gone from 64 X 64 to 2052 X 2052 in the last decade [Norton, 2002].

2.6 Multi- and Hyperspectral Arrays – GEN III

The third generation of HgCdTe devises is emerging and a definitive definition is not yet well established. In general it is taken to mean device structures that have substantially enhanced capabilities over the existing photodiode. Three examples are Two-Color Detectors, Avalanche Photodiodes, and Hyperspectral arrays. The key technical developments in these devices include dry etching, vapor-phase epitaxy, optical coatings, and advanced readout concepts. In IR systems, sensitivity in dual spectral bands has powerful discrimination capability. Dual band sensors have been demonstrated using two focal planes and a beam splitter. This technique is very difficult in optical alignment to a precision such that the exact same image feature can be accurately compared on the two focal planes at the pixel level. It also requires dual vacuum enclosures and cooling systems. Two color detectors are a remarkable solution to the problem of pixel registration in dual band sensors. Two color detectors are made with a stack of two detector layers separated by a common electrode. Although this structure can be grown using the liquid phase epitaxial growth method, as with photoconductors and photodiodes, the vapor phase growth technique is preferred. The development of anisotropic dry etching was important in being able to make these devices in smaller pixel sizes. The avalanche effect in the high-field region of an avalanche photodiode multiplies the number of photoexcited carriers by the avalanche gain. This raises the signal level, which itself may be highly useful for raising the low signal levels above the amplifier noise. When a second-generation array is combined in a scanning imager having a means to selectively illuminate each row with a different spectral band, the result is the ability to discriminate the objects in the scene based on

a spectral signature comprised of the unique reflectance spectrum of each band. When the devise can provide on the order of tens of spectral bands, it is called a Multispectral Imager. When the devise can image using hundreds of spectral bands, it is a Hyperspectral imager. Such instruments can image a scene in hundreds of spectral bands per frame, generating a hypercube image. Hyperspectral arrays have been built to cover the visible through LWIR spectral regions. HgCdTe and other detector materials such as silicon and InSb have been used in hyperspectral assemblies [Norton, 2002]. A Lincoln Laboratory prototype for a multipectral Advanced Land Imager (ALI) was launched in 2000 aboard the NASA Earth Observing (EO-1) satellite. EO-1 also carries a VNIR/SWIR hyperspectral sensor, called Hyperion, with 220 spectral bands and a ground sample distance (GSD) of 30 meters [Shaw, 2003].

CHAPTER III
PRINCIPLES OF INFRARED SYSTEMS

This chapter is based on the *Fundamentals of Thermal Imaging Systems* course material developed by Mike Marquis of Raytheon Company (© 1993-2003) [Marquis, 2003], an unpublished work. The structure and content of this chapter follows the course material, from photon emission, atmospheric transmission, through the optics, to the detector system. Where possible, the original source is sited. The reader is encouraged to refer to the cited references for in-depth derivations where desired. Derivation of the laws, theorems, and equations are not presented here. The objective is to familiarize the reader with the origins, and present the useful equations used in IR systems analysis.

3.1 Radiation Theory

Understanding of infrared radiation theory is of paramount importance in the design of IR sensor systems. Radiation theory describes the principles of how a source emits radiation and photons that can be detected, either by the human eye or sensor systems. This section describes the functions and expressions that have impact on performance parameters of electro-optic and photonic devices.

3.1.1 Blackbody

Here we must understand the concept a blackbody. Blackbody functions deal with the design analysis and performance predictions of IR sensors and sources. A blackbody is defined as a perfect radiation source, in that it radiates the maximum number of photons per unit time from a unit area in a specified spectral interval into a hemispherical region that any body can radiate at the same temperature and under thermodynamic equilibrium. [Jha, 2000]

3.1.2 Planck's Law

The Planck distribution function plays a key role in computation of radiant emittance from a blackbody source as a function of temperature. In it's original form, the Planck radiation law describes

how much energy is emitted from an object in certain wavelength interval, at a given temperature. It is also normalized for area and time.

$$W_\lambda = \frac{joules}{\sec ond} \cdot \frac{1}{cm^2 \cdot \mu m} = \frac{W}{cm^2 \cdot \mu m} = \frac{C_1}{\lambda^5 (e^{C_2/\lambda T} - 1)}$$ [Dereniak, 1984]

where λ is the wavelength of interest in microns (μ or μm), C_1 is the *first radiation constant*, C_2 is the *second radiant constant*:

$C_1 = 2\pi hc^2 = 3.741832 \times 10^4$ W/cm^2
h = Planck's constant 6.626176×10^{-34} W sec^2
c = speed of light $2.99792438 \times 10^{10}$ cm sec^{-1}
$C_2 = hc/k = 1.438786 \times 10^4$ μm&K
k = Boltzman's constant 1.380662×10^{10} W sec K^{-1}

and *T* is the absolute temperature of the object in kelvins (K). W_λ is called the *spectral radiant emittance,* and is the most important parameter is designing an IR system to meet performance requirements [Jha, 2000]. The subscript λ denotes the spectral nature of the quantity. Calculated values of the spectral radiant emittance as a function of wavelength at given temperatures are plotted in Figure 3. Note that at longer wavelengths, there is less variation in the spectral radiant emittance. Conversely, there is much greater variation at shorter wavelengths, and even more significantly at 300 K (~ 80^o F), the temperature range of most source areas.

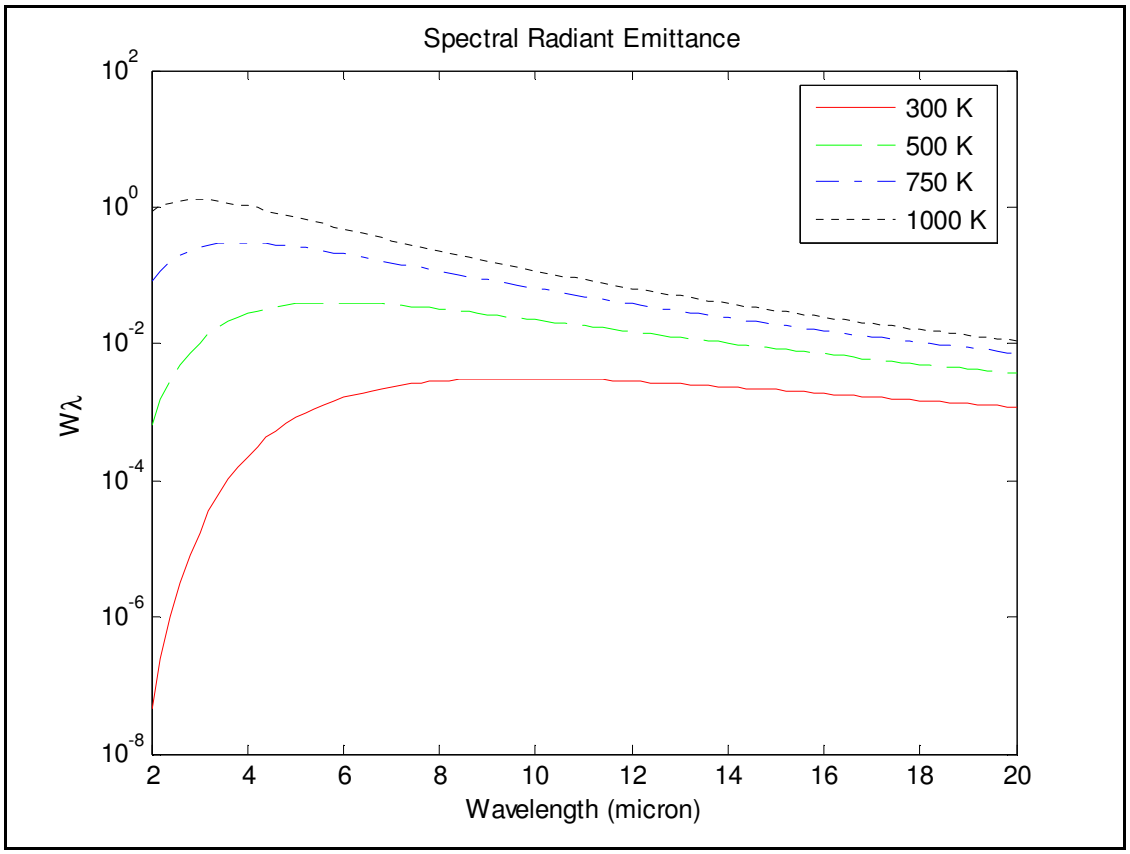

Figure 3. Spectral Radiant Emittance

3.1.3 Stefan-Boltzmann Law

W is called the *radiant emittance* and may be calculated by integrating W over all λ. W is also known as the Stefan-Boltzmann Law:

$$W = \int_0^\infty W_\lambda(T)\,d\lambda = \sigma T^4\ W/cm^2$$ [Dereniak, 1984]

where σ is the Stephan-Boltzmann constant:

σ = 5.60732 ❹$10^{-12}$ W/(cm^2&K^4)

Values of radiant emittance as a function of source temperature are plotted in Figure 4. We can estimate the radiant emittance from this curve for various sources operating at specific temperature. For example, a military jet's afterburners, with an approximated temperature of 2500 K, can expect radiant emittance of approximately 300 W/cm^2.

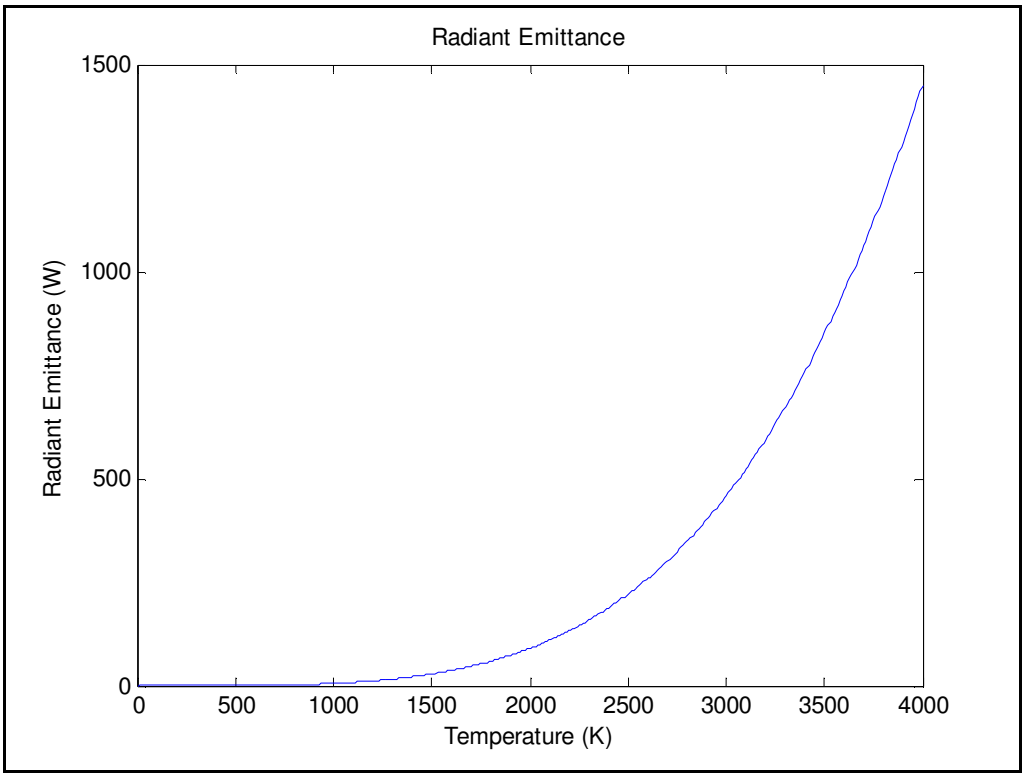

Figure 4. Radiant Emittance

In thermal imaging it is important to know how the amount of radiation emitted by an object varies given a small variation of the object temperature. Differentiating W_λ and W with respect to temperature results in the following equations.

$$\frac{\partial}{\partial T}W_\lambda = W_\lambda \frac{C_2 e^{C_2/\lambda T}}{\lambda T^2 (e^{C_2/\lambda T} - 1)} \frac{W}{cm^2 \cdot \mu m} K \qquad \text{[Marquis, 2003]}$$

$$\frac{d}{dT}W = 4\sigma T^3 W/(cm^2 \cdot K)$$

These results permit mapping the temperature differences in a scene to optical power differences propagating through space.

The roots of thermal imaging analysis are based on heat transfer laws because early detectors responded to the heating effect of the incident radiation. These detectors use the power forms of the radiation laws. However, now the temperature of most modern imaging detectors does not increase when

being irradiated by IR radiation. The radiation energy is absorbed by electron energy level transitions in crystals. An appropriate way to analyze this involves keeping track of radiation energy in terms of photons instead of joules. The energy of a photon is:

$$E = h\nu = \frac{hc}{\lambda} \text{ joules/photon} \qquad \text{[Dereniak, 1984]}$$

where h is Planck's constant, ν is time frequency, and c is the speed of light.

h = 6.626176 ❹ 10^{-34} joules/sec
c = 2.9979245 ❹$10^{14}$ μm/sec

The spectral radiant *photon* emittance can now be defined as:

$$Q_\lambda = \frac{W_\lambda}{hc/\lambda} = \frac{C_1/hc}{\lambda^4(e^{C_2/\lambda T}-1)} = \frac{C'}{\lambda^4(e^{C_2/\lambda T}-1)} \sec^{-1}\cdot cm^{-2}\cdot \mu m^{-1} \qquad \text{[Marquis, 2003]}$$

where C' = 1.88365 ❹$10^{23}$ $\sec^{-1}$ **&** cm^{-2} **&** μm^{-1}

The photon version of the Stefan-Boltzmann law, the total *photon* emittance is now:

$$Q = \int_0^\infty Q_\lambda(T)d\lambda = \sigma' T^3 \sec^{-1}\cdot cm^{-2} \qquad \text{[Marquis, 2003]}$$

where σ' = 1.52041 ❹$10^{11}$ $\sec^{-1}$**&**cm^{-2}**&**K^{-3}

3.1.4 Radiometric Terms

Radiometry is the science that measures the transfer of energy by electromagnetic radiative means. This also refers to infrared radiative energy transfer. The *rate of energy transfer* is referred to as the flux, or also power. *Radiant emittance* is the radiant flux emitted per unit area of a source. *Irradiance* is the radiant flux per area incident on a surface. *Radiant intensity* is the radiant flux per unit solid angle. *Radiance* is the radiant flux per unit solid angle per unit projected area [Marquis, 2003].

3.1.5 Lambert's Cosine Law

We assume a mirror perfectly reflects radiation, and the incident angle is equal to the reflected angle. It is called a specular reflector. For a diffuse surface, the incident angle does not equal the

reflected angle, but it reflects the incident radiation at random angles. For a perfectly diffuse reflector, the flux, or solid angle, is proportional to the cosine of the angle between the surface normal and the angle of observation. This angular distribution can also describe the flux distribution from or to a source. We usually assume that Lambert's cosine law holds:

$$W(\phi) = W(\phi = 0) \cdot \cos\phi$$

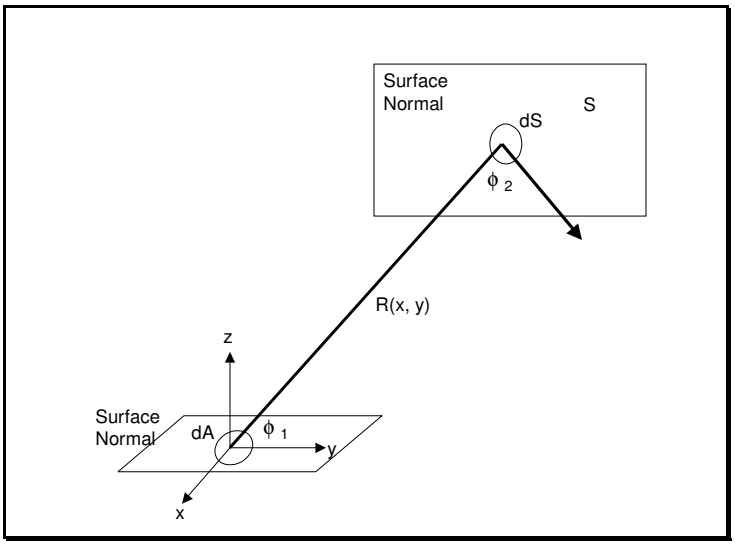

Figure 5. Radiation Exchange

Therefore, the radiation exchange, as shown in Figure 5 [Dereniak, 1984], between dA and S is proportional to the effective weighted solid angle.

$$\Omega = \int\int_{A} \frac{\cos\phi_1 \cos\phi_2}{R^2(x, y)} dS$$ [Marquis, 2003]

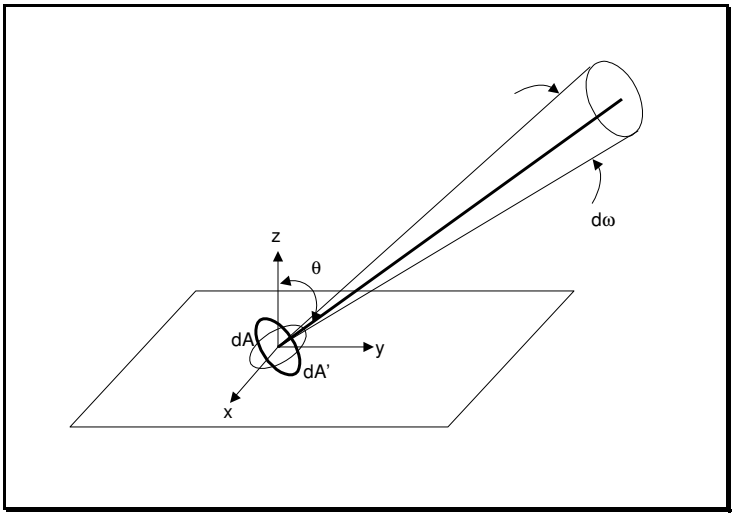

Figure 6. Radiance

The unit projected area in Figure 6 [Dereniak, 1984] is dA' = dAcosθ where dA is the area of the emitting surface. This defines the Radiance, N, the radiant flux (watts) per unit solid angle (steradians) per unit projected area (cm^2) as:

$$N = \frac{d^2 P}{d\omega dA \cos\theta} \quad \text{watts cm}^{-2}\text{sr}^{-1} \text{ (sr is steradians)} \qquad \text{[Marquis, 2003]}$$

Using this concept of the unit projected area allows analysis of irregular surfaces and of area that have no surface, such as the sky.

3.1.6 Kirchoff's Law

Finally it is important to understand Kirchoff' Law that describes the conservation of energy. The Planck radiation law assumes the source is a perfect blackbody. In real applications, there is no perfect blackbody. The Planck Law can still be used if we introduce a proportionality constant that relates the actual radiant emittance to the theoretical. This proportionality constant is called emissivity.

$$\varepsilon_\lambda W_\lambda(theoretical) = W_\lambda(actual)$$

Normally, the emissivity of a source is a function of wavelength. This is known as a Selective Radiator. If emissivity is constant for all wavelengths of interest, it is called a greybody. Applying Kirchoff's Law, there are three things that can happen to radiant energy incident on a surface. It can be

reflected, transmitted, or absorbed. Kirchoff's Law also implies that when energy radiance results from a radiative process, at thermal equilibrium, then we can say, "good absorbers are good emitters". The ratios of these energies are called reflectance (ρ), transmittance (α) and absorptance (τ).

$$\rho = \frac{energy\ reflected}{energy\ incident}$$
$$\alpha = \frac{energy\ absorbed}{energy\ incident}$$
$$\tau = \frac{energy\ transmitted}{energy\ incident}$$
$$\rho + \alpha + \tau = 1$$ [Dereniak, 1984]

3.2 Atmospheric Transmission

Transmission of IR radiation in the atmosphere is very complex due to the dependence of scattering and absorption effects on a number of physical properties of the atmosphere. Scattering is caused by the presence of obscurants, such as dust, smoke, fog, and rain. Atmospheric absorption is caused mostly by the presence of molecule absorption bonds and is strictly a function of wavelength. The amount of attenuation introduced by atmospheric absorption and scattering is an important factor in the design of IR sensors. Atmospheric attenuation reduces system performance. In the case of target tracking and target acquisition, molecules could seriously degrade system performance to the point of mission failure. [Jha, 2000]

The earth's atmosphere is not uniformly transparent for all wavelengths or all wavelength intervals, with some being very opaque. The spectral regions over which it is transparent for significant distances are known as *atmospheric windows* as shown in Figure 7 [Groves, 2002].

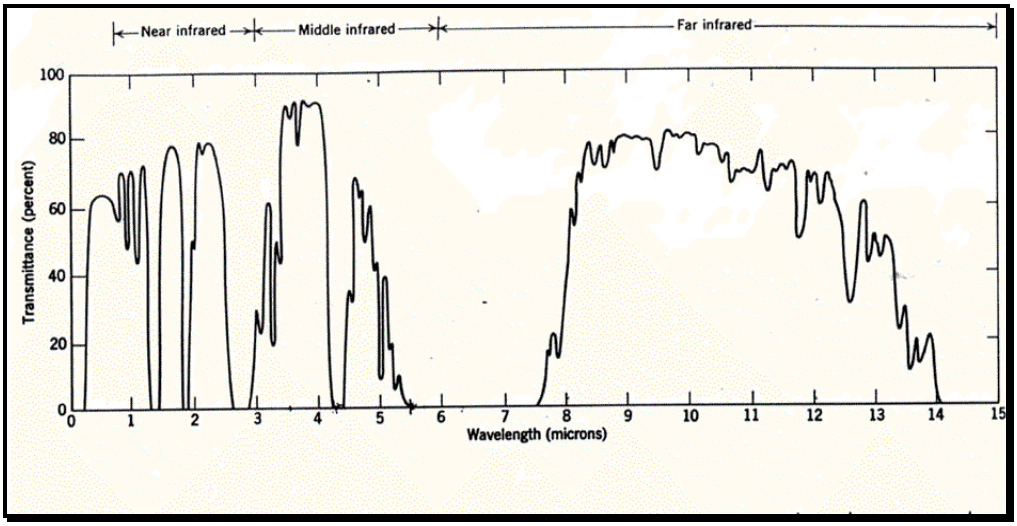

Figure 7. Atmospheric Windows

The spectral transmission, in a gaseous atmosphere for a given path is reduced by several factors such as wavelength, path length, pressure, temperature, humidity, and the chemical composition of the atmosphere. To simplify the complexity of this problem, if the amount of energy (E) lost over the distance traveled (R) is proportional to the original energy, then this can be express by the differential equation:

$$\frac{dE_\lambda}{dR} = -\sigma_\lambda E_\lambda \quad \text{or} \quad \frac{dE_\lambda}{E_\lambda} = -\sigma_\lambda dR \quad \text{where } \sigma \text{ is a proportionality parameter}$$

$$\int \frac{dE_\lambda}{E_\lambda} = -\int \sigma_\lambda dR$$

$$\ln E = -\sigma_\lambda R + c$$

$$E_\lambda = e^{-(\sigma_\lambda R + c)} \qquad \text{At R = 0, } E_\lambda = E_{0\lambda}$$

$$\frac{E_\lambda}{E_{0\lambda}} = \tau_\lambda(R) = e^{-\sigma_\lambda R} \qquad \text{[Jha, 2000]}$$

This atmospheric transmittance law is known as "Beer's Law". The proportionality parameter is known as the *extinction coefficient* or the *spectral attenuation coefficient*, with its units of km^{-1}. The extinction coefficient for a given wavelength is broken down in to several components to account for the loss of energy.

$$\sigma_\lambda = \alpha_\lambda + \rho_\lambda + \phi_\lambda + \gamma_\lambda$$ [Jha, 2000]

where α is absorption, ρ is reflection, ϕ is diffraction, and γ is scattering. Assuming negligible contribution from diffraction and reflection, the extinction coefficient is reduced to

$$\sigma_\lambda = \alpha_\lambda + \gamma_\lambda$$ [Jha, 2000]

3.2.1 Absorption

Absorption due to water vapor, carbon dioxide, and ozone make up 95% of the absorption coefficient, with other atmospheric elements being negligible. Ozone absorption is most pronounced in the ultraviolet region of the spectrum and is negligible at longer radiation wavelengths exceeding 8 μm.

3.2.2 Scattering

Scattering effects are dependent on both wavelength and the size of the particles in the atmosphere. Scattering is described by understanding what happens to the radiant energy as it passes near the particle. Some of the energy penetrates the particle, with some of that energy passing through, and some energy lost to absorption and some to internal reflection. Other energy is reflected and diffracted from the particle. The results of scattering on visible light can be seen in several everyday situations. A common example is a blue sky during the day and a reddish sky during sunset. During the day, the sun's light travels through less of the earth's atmosphere to reach our eye. The shorter wavelengths of the blue portion of the spectrum are not affected. But, as the sun sets and approaches the horizon, the light must pass through much more of the earth's atmosphere to reach our eye. Scattering affects the blue wavelengths, resulting in poorer penetration, while the longer wavelengths of red light is less affected, resulting in better penetration and causing the sky to appear more red.

3.2.3 Mie and Rayleigh Scattering

If all the scattering particles are the same size, the Mie scattering formulas are applied. Mie scattering formulas are derived from the solution of Maxwell's equations. The Mie scattering theory gives rise to the scattering area ratio, denoted as K. In general, K = 2. However, as the size of the particles approaches the given wavelength, K is a ratio of particle radius to wavelength, K = f(r/λ). When r/λ is less than 1, the fastest change of K occurs. This region is known as Rayleigh scattering. The Rayleigh scattering coefficient is proportional to $1/\lambda^4$. When r/λ is greater than 1, the result is Mie scattering and is much less sensitive to changes in r/λ. When all particles are the same size, the scattering cross-section (πr^2) is related to the scattering coefficient by

$\gamma_\lambda = \pi n K r^2$ where n is the number of droplets per volume

Atmospheric gaseous molecules are about the same size as visible wavelengths. Therefore, Rayleigh scattering is predominating. But, since IR wavelengths are much longer, atmospheric gaseous molecules have little scattering effect. Fog and cloud droplets are very large compared to visible and IR wavelengths and are subject to Mie scattering, making them appear white and opaque. That is why some IR sensors are not all weather. Scattering and absorption affect what we know as contrast. It is the contrast of an object and it's surroundings that are of importance in IR sensor design, and predicting performance. If the size distribution of a scattering aerosol is know, as well as the composition of the aerosol, the application of Mie theory results in γ_λ. However, the composition of the aerosol is almost never known. There are empirical methods to determine γ_λ. In the visible spectrum,

$$\bar{\tau}_{vis}(R) = e^{-(\alpha_{vis}+\gamma_{vis})R} \approx e^{-\gamma_{vis}R}$$ [Marquis, 2003]

If we know the meteorological range, and given a required contrast of 2%, we can use the Koschmieder relation to estimate γ_{vis}.

$$\gamma_{vis} = \frac{-\ln 0.02}{R_{met}} = \frac{3.912}{R_{met}}$$

From this relationship of the scattering coefficient for the visible spectrum (0.3 μm to 0.72 μm), several empirical laws have been attempted to determine the scattering coefficient for the IR spectrum. One method, used in "EOSAEL" is

$$\log \gamma_{IR} = a + b \log \gamma_{vis}$$

where a and b are coefficients that depend on the air mass and the spectral band of operation. The values of a and b, determined empirically for the 8 to 12 band are shown in Table 1.

Table 1. Scattering Coefficients

Air Mass	A	B
Maritime Artic	-0.45	1.19
Maritime Polar	-1.01	1.51
Continental Polar	-1.65	1.82

3.2.4 Beer's Law

For military applications, other scattering effects must be considered. These are known as battlefield obscurants and have different properties than those described above for the atmosphere. Battlefield obscurants include white phosphorus smoke, fog oil and dust created from impacting artillery shells. The effects of this type of obscurants are transient and initially localized. They also tend to spread, or dissipate over time. The transmission is predicted by Beer's law.

$$\tau = e^{-\alpha CL} \qquad \text{[Marquis, 2003]}$$

where α is the mass extinction coefficient in units of m^2/g, and CL is the concentration length product in g/m^2. Table 2 shows representative values of α for these battlefield obscurants. Again here, we see that longer wavelengths penetrate obscurants more effectively.

Table 2. Mass Extinction Coefficients

	Wavelength (μm)				
	Visible	**Near IR**	**Medium IR**	**Far IR**	**Laser**
Obscurant	**0.4-0.7**	**1.06**	**3-7**	**8-12**	**10.6**
Fog oil	6.85	3.48	0.25	0.02	0.02
White Phosphorus	4.08	1.37	0.29	0.38	0.38
Artillery Dust	0.24	0.24	0.24	0.24	0.24

3.2.5 Transmission Analysis

To this point we have characterized the radiant emittance and properties of a target and the factors that effect the transmission of that radiance through the atmosphere. Now we must determine which spectral band in which to operate. There is no easy solution. The answer depends on parameters that vary with respect to the spectrum of the operating environment. These parameters include the target signature, the target's contrast to its background, atmospheric transmission, and sensor response resulting from its optics and detector. If the sensor response can be assumed to be Background Limited Performance (BLIP), the transmission can be analyzed using the function

$$R_{\Delta T} = \frac{1}{2\sqrt{2hc}} \bullet \frac{\int_0^\infty \lambda T_F(\lambda) T_a(\lambda) \frac{\partial W_\lambda}{\partial T} d\lambda}{\sqrt{\int_0^\infty T_F(\lambda) Q_\lambda d\lambda}} \qquad \text{[Marquis, 2003]}$$

This equation represents the signal-to-noise ratio of a 1-degree target signature in an ambient 300 K (80^o F) environment.

3.3 Optics

There are two basic categories of an optical system, either reflective or refractive. For a particlar system, choosing between the two types of optics depends on several factors of the design. Each has merits and drawbacks. A reflective system requires less volume. The materials, fabrication, and alignment of a reflector also result in less production costs. However, a refractor gives more flexibility in design since folds in the beam path can be placed is arbitrary positions. Multispectral sensors would favor the use of reflectors. For a specific lens diameter and focal length, the reflective and absorption losses for a refractor will be greater than the absorption losses of a reflector, but the overall collection efficiency of the reflector may or may not be better depending on the amount of central obscuration. A

reflector tends to be lighter in weight and less expensive than an equivalently sized refractor, but the reflector may not have the same image quality. FLIR designs favor refractive optics. In most cases, to meet performance specifications, a combination of both reflective and refractive optics are used. These systems are called catadioptric [Marquis, 2003].

In the idealized processes, refraction occurs at the interface between two nonconducting transparent media. Reflection occurs at the surface of a perfect conductor such as a mirror. Figure 8(a) [Lloyd, 1975] shows the interface between two conductive materials, each characterized by a refractive index *n*, which is the ratio of the speed of light in the material to the speed of light in a vacuum.

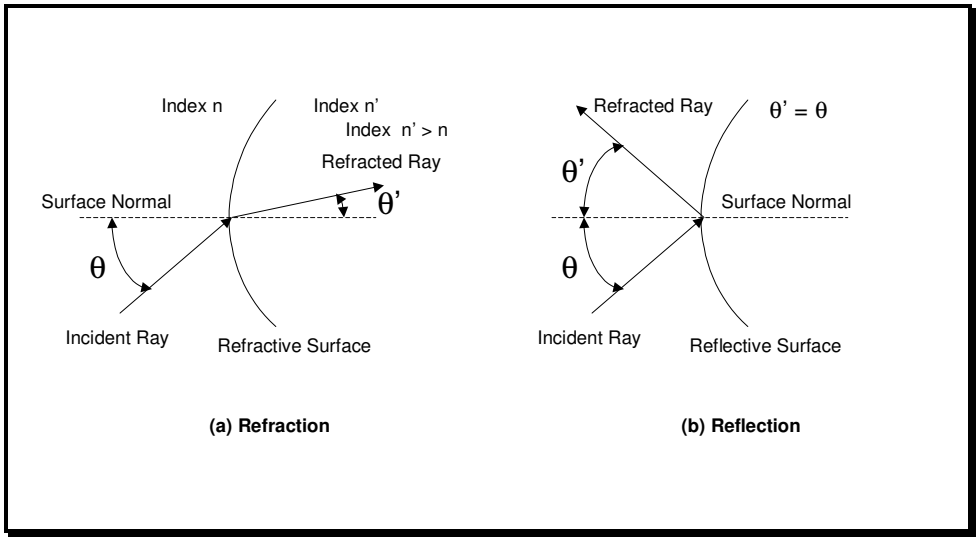

Figure 8. Refraction and Reflection

Figure 8(b) shows the reflection of a perfect conductor (a mirror). For nonmagnetic materials, n is the square root of the dielectric constant evaluated at the optical frequency of interest. This demonstrates Snell's law of refraction, which is that for angles of incidence θ and of refraction θ' measured from the surface normal, and for refractive indices n and n'

$$\frac{\sin\theta'}{\sin\theta} = \frac{n}{n'} \quad \text{or} \quad \theta = \arcsin\left(\frac{n}{n'}\sin\theta\right) \qquad \text{[Lloyd, 1975]}$$

A simple optical system can be characterized as a single spherically shaped lens as shown in Figure 9 [Lloyd, 1975], defined by four parameters: the radii of curvature R_1 and R_2, the thickness t, and the index of refraction n. When the thickness is negligible, it is considered a thin lens.

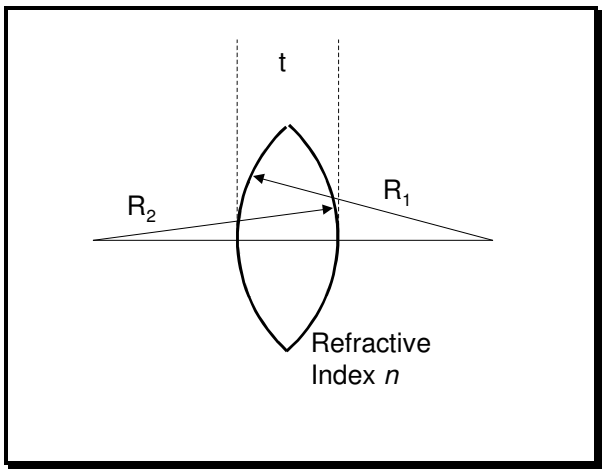

Figure 9. Simple Lens

Ray trace techniques are used to analyze optical systems. Consider parallel light beams passing through the lens. The refraction of the material causes the light to bend as it passes through the lens. The point at which the light converges is called the focal point and defines the location of the focal plane. This quantity is shown in Figure 10 [Lloyd, 1975]. In a simple lens, when the refractive index is known, the focal length can be found by

$$f = \frac{R_1 R_2}{(n-1)(R_2 - R_1)}$$ [Lloyd, 1975]

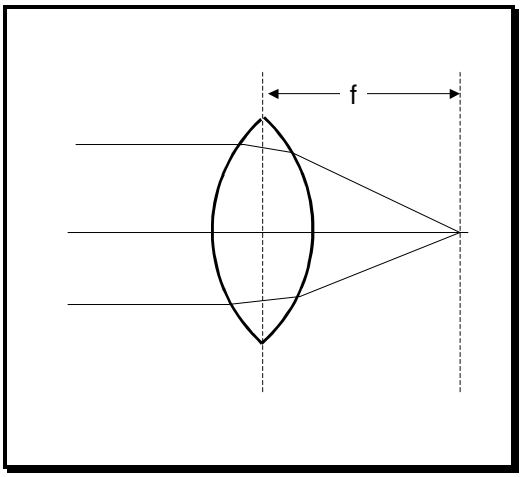

Figure 10. Focal Length

The importance of the magnitude of the refractive index of a potential lens material is evident from this equation. The higher the index, the larger the radii may be for a particular focal length. This makes it easier to manufacture and to uniformly coat the lens to reduce reflection, and makes the lens thinner, giving less absorption loss.

Figure 11 [Rogatto, 1993] shows a generalized optical system to illustrate key definitions in optical design. If each light ray, incident on the optical system parallel to the axis, is extended to meet the backward extension of the same ray after it passes through the system, the focus of the intersections of all the rays is called the *principal plane*. Rays from the right form the *first principal plane*. The *second principal plane* is formed by rays incident from the left. The principle planes are planes only in the paraxial region; at any finite distance from the axis they are figures of rotation, frequently approximating spherical surfaces. The intersections of the principle planes with the optical axis are the *principal points*. The *focal point* is the point at which rays, parallel to the to the axis, converge, or appear to converge after passing through the optical system. The *front* or *first focal point* is the point to which rays incident from the right converge. Likewise, the *back* or *second focal point* is the point at which rays incident from the left converge. The *front focal length* (FFL) is the distance from the front focal point to the optical system. The *back focal length* (BFL) is the distance from the back focal point to the optical system. The *equivalent focal length* (EFL) is the distance from the back focal point to the second principal point.

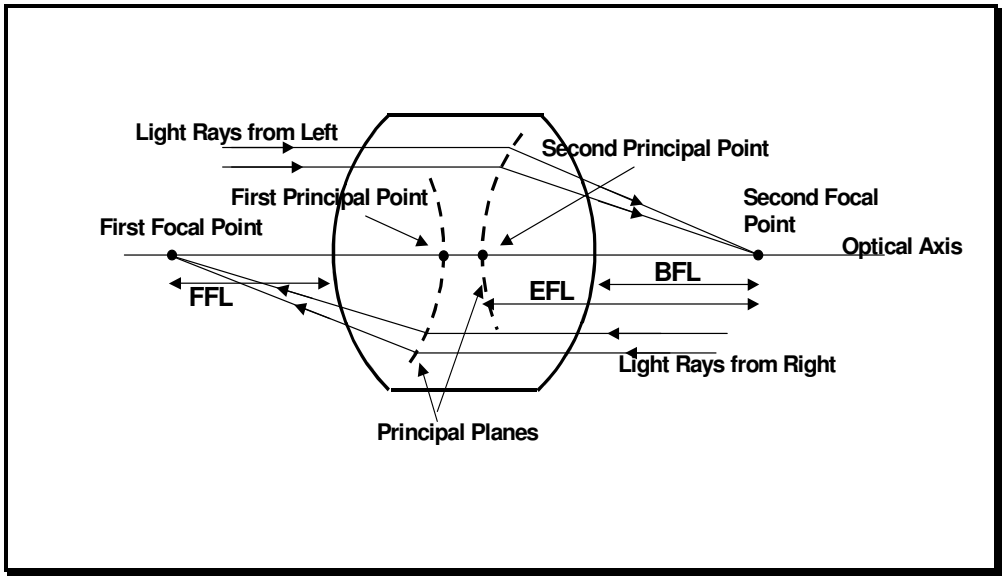

Figure 11. Generalized Optical System

For complex systems, sign conventions are established to assist in evaluating key parameters. Light rays are assumed to progress from left to right. Radii and curvatures are positive if the center of curvature is to the right of the surface. Surfaces or elements have positive power if they converge light. Distances upward or to the right are positive, that is, points that lie above the axis or to the right of an element, surface, or another point are considered to be a positive distance away. Slope angles are positive if the ray is rotated counterclockwise to reach the axis. Angles of incidence, refraction, and reflection are positive if the ray is rotated clockwise to reach the normal to the surface. The index of refraction is positive when the light travels in the normal left-to-right direction. When the light travels from right to left, for instance, after a reflection, the index is taken a negative [Rogatto, 1993].

For simple or complex systems, we can apply the following equations. Although these relationships are exact for only a thin, thread-like, infinitesimal region near the optical axis, most well corrected systems closely approximate these relationships. Figure 12 [Rogatto, 1993] shows the positional relationships. The Image Position is expressed by

$$\frac{1}{s'} = \frac{1}{s} + \frac{1}{f}$$

$$x' = -\frac{f^2}{x}$$

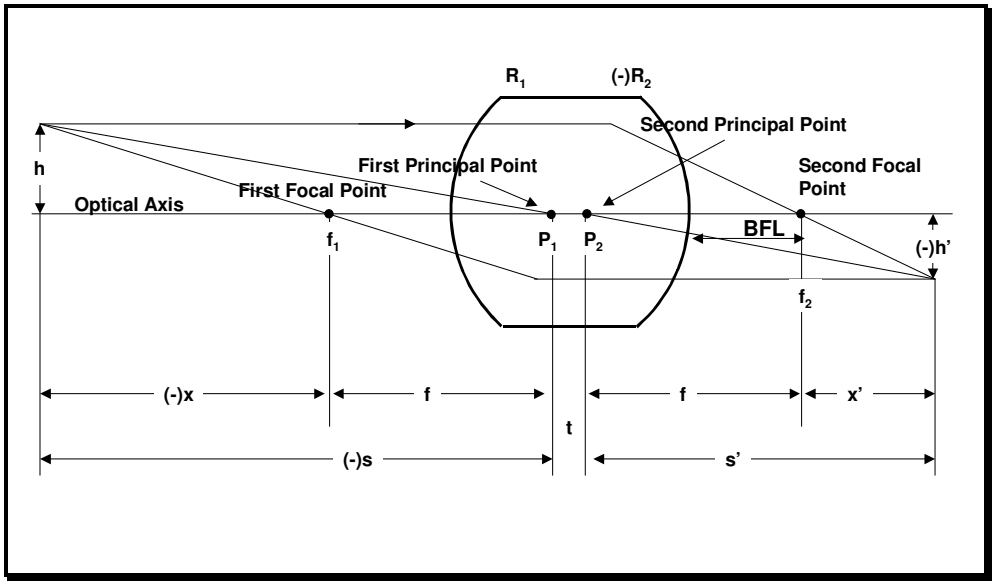

Figure 12. Object and Image Relationship

The lateral magnification of the image can be expressed by several ratios:

$$m = \frac{h'}{h} = \frac{s'}{s} = \frac{f}{x} = -\frac{x'}{f}$$

The longitudinal magnification is m^2. The power ϕ, focal length, and back focal length are:

$$\phi = \frac{1}{f} = (n-1)\left[\frac{1}{R_1} - \frac{1}{R_2} + \frac{t(n-1)}{nR_1R_2}\right]$$

$$BFL = f\left[1 - \frac{t(n-1)}{nR_1}\right]$$

From the focal length equation above, we can see how a negligible thickness reduces to

$$\phi = \frac{1}{f} = \frac{(n-1)(R_2 - R_1)}{R_1R_2}$$

as shown previously.

When a system consists of two components, *a* and *b* as shown in Figure 13 [Rogatto, 1993], the following expressions may be applied. The components *a* and *b* may be simple elements, mirrors, compound lenses or individual complex systems.

$$\phi_{ab} = \frac{1}{F_{ab}} = \phi_a + \phi_b - d\phi_a\phi_b = \frac{1}{F_a} + \frac{1}{F_b} - \frac{d}{F_a F_b}$$

$$F_{ab} = EFL_{ab} = \frac{F_a F_b}{F_a + F_b - d}$$

$$BFL_{ab} = F_b\left(\frac{F_a - d}{F_a + F_b - d}\right) = F_{ab}\left(\frac{F_a - d}{F_a}\right)$$

$$-FFL = F_{ab}\left(\frac{F_b - d}{F_b}\right)$$

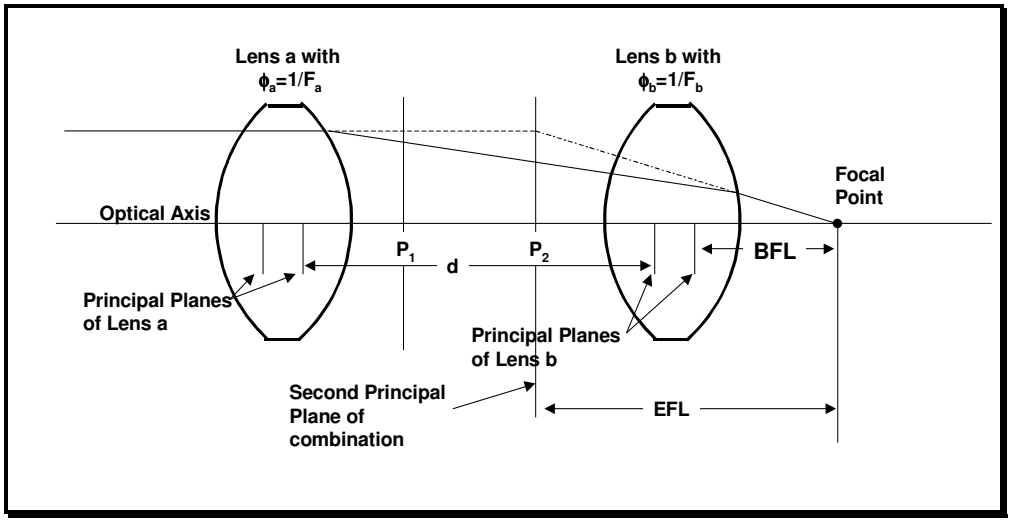

Figure 13. Two-Component System

Form these equations we can determine the set of characteristics of the components to achieve the desired powers.

$$F_a = d\left(\frac{F_{ab}}{F_{ab} - BFL}\right)$$

$$F_b = -d\left(\frac{BFL}{F_{ab} - BFL - d}\right)$$

$$d = F_b\left(\frac{BFL}{F_b - BFL}\right) = F_a + F_b - \frac{F_a F_b}{F_{ab}}$$

3.4 Optical Performance

A key input to the optical design is how well the system should form an image. This measure of "goodness" is difficult to quantify. The image should appear as the object does, should have sharpness, some color fidelity, and be undistorted, to name a few characteristics. When considering the thermal imaging system, an appropriate measure would be one that indicates improved performance for the observer. That is, use of the IR system should improve the observer's ability to discriminate the desired target from its surroundings that the observer would otherwise be able to achieve. In general, this has been accepted to mean a higher *resolution*. However, resolution, or the ability to discriminate fine detail is still not rigorous enough [Marquis, 2003]. There are several definitions of resolution and image quality developed by Rayleigh, Sparrow, and Strehl (see Rogatto, 1993) and others. A useful measure of imaging quality has emerged that is based in the rigorous mathematics of linearity. A system is considered linear if

$f(x) = y$, and $f(ax) = ay$, and $f(x+a) = f(x) + f(a)$

From this, the Convolution Theorem proves

$$\mathsf{F}\left[\int_{-\infty}^{\infty} f(x)g(\tau - x)dx\right] = F(X)\cdot G(X)$$

which implies that convolution in one domain is equivalent to multiplication in the transformed domain. In order for an optical system to replicate fine image detail, it must possess good response at high spatial frequencies. The spatial frequency response of an optical system can be found using Fourier transforms. The optical transfer function (OTF) of an imaging system is the Fourier transform of its impulse response. An impulse in an optical system is a space delta function. The spatial frequency dimension is cycles per linear dimension, normally cycles/mm at the focal plane, and is orientation dependent in the horizontal, vertical, or other angular dimension. Since the range to the object is often not know, a more convenient measure in the object space is angular, or cycles/milliradian.

A two-dimensional spatial impulse, such as a bright star, can be thought of as a point. Since optical systems spread out the image of a point, the optical system response is called the point spread function (PSF). The Fourier transform of a system's PSF is called the optical transfer function (OTF), and is generally a complex number:

$$\mathbb{F}\,(\mathrm{PSF}) = \mathrm{OTF}(f_x) = \mathrm{MTF}(f_x)e^{-j\mathrm{PTF}(fx)} \qquad \text{[Dudzik, 1993]}$$

where MTF is the modulation transform function, PTF is the phase transfer function, and f_x is spatial frequency in cycles/milliradian.

Optical system imaging is a good approximation of a convolutionary process. The individual point spread functions of the optical components must be convolved to result in the point spread function of the system. Because of the complexity of thermal imaging systems, convolutionary processes do not fully describe their behavior. However, this approximation is adequate in at least one orientation of the image [Marquis, 2003]. For a more complete description of transfer functions see Rogatto, 1993. For the purposes of this report, it is sufficient for the reader to comprehend the convolution and modulation transfer functions, and that the MTF transforms the optical image in the frequency domain to the spatial domain. Additionally, MTF represents a loss of image quality from the original object. Modulation is a measure of the relation between the dimmest and brightest portions of the scene and the average level. It is one measure of what is commonly called contrast. Modulation of radiance is defined as:

$$modulation = \frac{L_{\max} - L_{\min}}{L_{\max} + L_{\min}}$$

The modulation transfer is the ratio of modulation in the image to that in the object:

$$MT = \frac{\left(\dfrac{L_{\max} - L_{\min}}{L_{\max} + L_{\min}}\right)image}{\left(\dfrac{L_{\max} - L_{\min}}{L_{\max} + L_{\min}}\right)object}$$

The maximum value is one, and the minimum is zero. It is never negative. In the infrared, the modulation is differences in emissivity and temperature. The MT of the system is the product of the component MTs, or

$$MT_{system}(f_x) = \prod_{i=1}^{n} MT_i(f_x).$$

As will be shown is the next chapter, IR systems are complex, with several components. Each component adds to the MTF loss of the overall system. Signal processing and software algorithms aid to compensate for the loss in image quality.

3.5 Infrared Detectors

The responsive element of an IR detector is a radiation transducer. It changes the incoming radiation into electrical power that is then amplified by the accompanying electronics. The method of transduction is separated into two groups: Thermal detectors and photon detectors. The responsive element of thermal detectors is sensitive to changes in temperature brought about by changes in incident radiation. The responsive element of photon detectors is sensitive to changes in the number of free charge carriers, i.e., electrons and/or holes that are brought about by changes in the number of incident infrared photons. Thermal detectors employ transduction processes including the bolometric, thermovoltaic, thermopneumatic, and pyroelectric effects. Photon detectors employ transduction processes including the photovoltaic, photoconductive, photoelectromagnetic, and photoemissive effects [Rogatto, 1993].

Windows are used to isolate the ambient environment from the special environment often required around the responsive element. In cooled detectors, the responsive element is kept in a vacuum. The window affects the spectral distribution of photon incident on the responsive element. Apertures are used to restrict the field of view of the responsive element. This is often done in cooled detectors that are photon-noise limited to cut down on the extraneous background photons and thus reduce noise. A dewar is a vessel having double walls, the space between being evacuated to prevent the transfer of heat, and the

surfaces facing the vacuum being heat reflective. Dewar flasks are used to house the coolant needed to reduce the operating temperature of the responsive element and thus improve detectivity [Rogatto, 1993].

3.5.1 Figures of Merit

Figures of merit are used to compare the measured performance of one detector against another of the same class, the performance required to perform a given task, or the calculated performance expected of an ideal detector that performs at a level limited by some fundamental physical principle. Care in the use of detector figures of merit is essential because many parameters of detector performance do not fully summarize the relevant factors in detector choice. The engineer of detector systems should therefore understand the definitions and limitations of commonly used figures of merit [Dereniak, 1884].

3.5.1.1 Responsivity

A basic figure of merit that applies to all detectors with electrical output is responsivity, denoted by R, which is the ratio of the output, usually in amperes or volts, to the radiant input in watts. The spectral voltage responsivity of a detector at a given wavelength λ is the measured voltage output (V_s), divided by the spectral radiant power incident on the detector ($\phi_e(\lambda)$), or

$$\Re_V(\lambda, f) = \frac{V_s}{\phi_e(\lambda)} \qquad \text{[Dereniak, 1984]}$$

The blackbody responsivity R(T, f), is the detector output divided by the incident radiant power from a blackbody source of temperature *T* modulated at a frequency *f* that produces the observed output:

$$\Re_V(T, f) = \frac{Vs}{\int_0^{\alpha} \phi(\lambda) d\lambda} = \frac{V_s}{A_s \sigma_e T^4 A_d / \pi R^2} \qquad \text{[Dereniak, 1984]}$$

where A_d is the detector area, irradiated by a blackbody of temperature *T* of area A_s at a distance *R*. It is implicit in the above equation that the source and detector are both normal to the optical axis. The equation also holds if the detector is preceded by an optical system that images all of the source area onto the detector area without loss to noise. Note that the blackbody responsivity is a measure of the detector

response to the incident radiation integrated over all wavelengths, even though the detector is sensitive to only a finite wavelength interval.

3.5.1.2 Noise Equivalent Power

The noise equivalent power (NEP) of a detector is the required power incident on the detector to produce a signal output equal to the root-mean-square (rms) noise output. In other words, NEP is the signal level that produces a signal-to-noise ratio of 1 [Dereniak, 1984]. The smallest signal that a transducer may faithfully reproduce is ultimately limited by the noise inherent in the transformation process. It is convenient to assume that the transducer is noiseless and that the observed noise results from a noisy input signal [Marquis, 2003]. The current signal output is

$$i_s = \Re_i \phi_e \qquad \text{[Dereniak, 1984]}$$

so the signal-to-noise ratio is

$$S/N = \frac{\Re_i \phi_e}{i_{rms}} \qquad \text{[Dereniak, 1984]}$$

The NEP is the incident radiant power, ϕ_e, for a signal-to-noise ratio of 1, or

$$1 = \frac{\Re_i NEP}{i_{rms}}, \text{ and solving for NEP: } NEP = \frac{i_{rms}}{\Re_i} \qquad \text{[Dereniak, 1984]}$$

where i_{rms} is the root-mean-square noise current in amperes and $\mathrm{R_i}$ is the current responsivity in amperes per watt. Either the spectral responsivity $R_i(\lambda, f)$ or the blackbody responsivity $R_i(T, f)$ may be inserted into the above equation to define two different NEPs. The spectral NEP, $NEP(\lambda, f)$ is the monochromatic radiant flux $\phi_e(\lambda)$ required to produce an rms signal-to-noise ration of 1 at frequency *f*. The blackbody NEP, *NEP(T, f)*, is the blackbody radiant flux required to produce an rms signal-to-noise ratio of 1. The NEP is a useful parameter for comparing similar detectors that operate under identical conditions. But, it should not be used as a summary measure of detector performance for comparing dissimilar detectors. It can be shown that the larger the bandwidth Δf, the larger the noise that is present. This would increase NEP. The blackbody responsivity $\mathrm{R_v}$(T, f) implies that increasing the detector area,

A_d, will decrease the responsivity if all other factors are held constant. From the NEP equation above, it may be concluded that a decrease in responsivity will increase the NEP. It is seen, then, that both A_d and Δf influence the NEP in the same direction. However, neither the detector area nor the bandwidth was specified in the definition of NEP. A comparison of NEPs measured under different conditions can therefore be misleading [Dereniak, 1984].

3.5.1.3 Detectivity

The detectivity of a detector is simply the reciprocal of the noise equivalent power:

$$D = \frac{1}{NEP}$$ [Dereniak, 1984]

Good detectors have a small NEP. That is counterintuitive for most people. The equivalent figure of merit that gives larger values for a more-sensitive detector ("bigger is better") is detectivity. A more useful figure of merit is D* (dee-star) which is normalized for detector area and bandwidth:

$$D^* = \frac{\sqrt{A_d \Delta f}}{NEP}$$ [Dereniak, 1984]

The advantage of D* as a figure of merit is that it is normalized to an active detector area of 1 cm^2, a noise bandwidth of 1 Hz, and is illuminated with 1 watt of optical power. Therefore, D* may be used to compare directly the merit of detectors of different size whose performance was measured using different bandwidths [Dereniak, 1984]. Typical values of D* are from 10^8 to 10^{12}.

3.5.1.4 Quantum Efficiency

Quantum efficiency denoted by η_Q is the probability that a photoelectron is produced when a photon is incident on the detector, or the fraction of photons incident on a detector that create a response. It is largely a function of geometry, surface reflection, and the bulk absorption of the detector material [Marquis, 2003]. The quantum efficiency of a conventional detector is dependant on the absorption coefficient of the semiconductor material deposited and is directly proportional to the thickness of the active regions. However, thicker active regions tend to reduce device speed and response time due to long transmit time. Placing the active devise structure inside an optical resonant microcavity can

significantly increase photon detector performance. Figure 14 [Marquis, 2003] shows an example of this structure and illustrates the quantum efficiency equation.

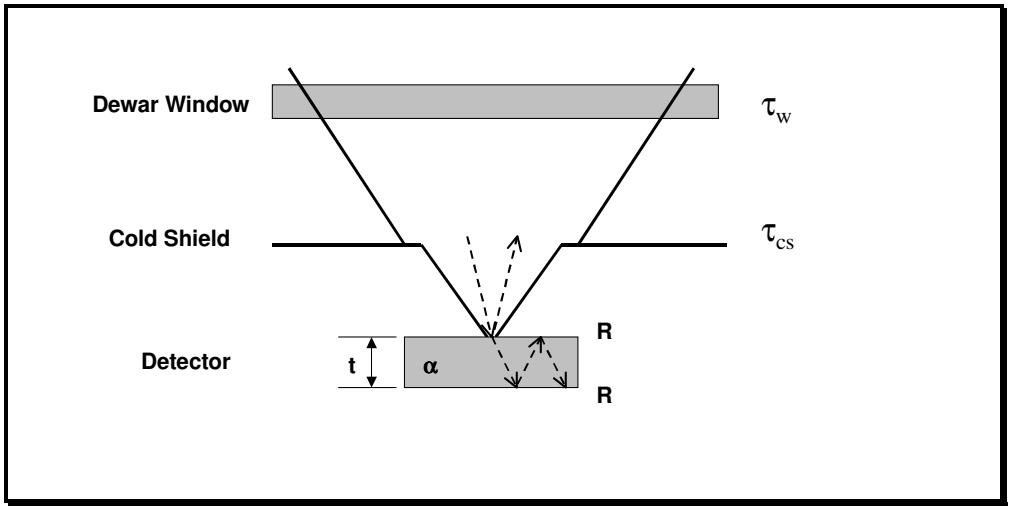

Figure 14. Quantum Efficiency

The quantum efficiency of a detector is given by:

$$\eta_Q = \tau_w \tau_{cs} \frac{(1-R)(1-e^{-\alpha t})}{1-\mathrm{Re}^{-\alpha t}}$$ [Marquis, 1999]

Where *(1-R)* is the fraction through the detector front surface, $(1-e^{-\alpha t})$ is the first pass amount not absorbed, $(1-Re^{-\alpha t})$ is the fraction absorbed during multiple internal reflections, τ_w is the fraction passed through the Deware Window, τ_{cs} is the part not lost due to cold shielding vignetting, R is the reflectivity of the detector surface, α is the detector material absorption coefficient and t is the thickness of the detector. Desired values of η_Q are 80% to 90% [Marquis, 2003]. The loss in quantum efficiency from the ideal value of 1 is due to:

- Optical reflection losses.
- Surface traps or recombination centers.
- Absorption coefficient varying as a function of wavelength.
- Photogenerated carriers being created further than a diffusion length from the depletion region.

3.5.2 Detector Noise

The noise level of the detector determines the limit of sensitivity, and it must be considered in order to determine the detectable incident power. The noises that are present in a photoconductive application are 1/*f* noise, Johnson noise, and generation-recombination (photon) noise. The 1/*f* noise is dominant at low frequencies, generation-recombination noise is dominates at midband, and Johnson noise dominates the high frequencies. This relationship is depicted in Figure 15 [Dereniak, 1984; Marquis, 2003], a mean square noise power spectral density curve. The transition frequencies from one type of noise to another varies with the detector material used. Additionally, the 1/*f* to generation-recombination transition varies between detectors of the same material, known as the "knee". For example, it can vary from 5 to 200 Hz for doped silicon and HgCdTe detectors depending on contact technology and techniques used in fabrication. The carrier lifetime break point is typically near 1 MHz, which again varies for various types of detectors [Dereniak, 1984].

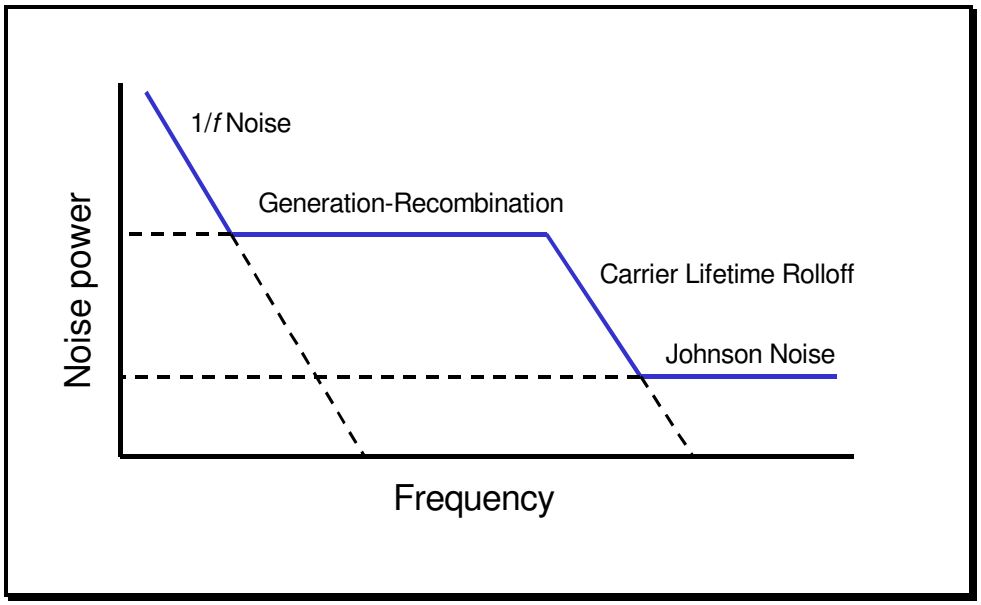

Figure 15. Noise Power Spectral Density Curve

3.5.2.1 1/*f* Noise

The physical mechanism that produces this noise source is not well understood. The 1/*f* dependence, higher noise level at lower frequency, holds for the noise power, the noise voltage varying as one over the square root of the frequency. Since photoconductors require a bias current, there will always be 1/*f* noise present. The following equation has been empirically obtained for the mean square noise current

$$i_{1/f}^2 = \frac{B_1 I_b^2 \Delta f}{f^\beta}$$ [Dereniak, 1984]

where B_1 is the proportionality constant, I_b is the DC current through the detector, Δf is the electrical bandwidth, f is frequency, β is a constant, usually 1. For a photoconductor at low frequencies, the dominant noise exhibits the 1/*f* dependence. As the frequency of interest is increased, this component drops below the generation-recombination or the Johnson noise for low photon flux and cryogenic cooled detectors. The 1/*f* noise component does not present a fundamental limit to sensitivity. Careful surface preparation and electrical contacting methods reduce this noise to negligible levels. In any case, the development of a low 1/*f* noise photoconductor remains an art rather than a science [Dereniak, 1984].

3.5.2.2 Johnson Noise

Johnson noise is caused by the thermal agitation of electrons in a resistor. It is also called Nyquist or thermal noise, but is often called Johnson noise after the scientist who discovered it (see Johnson, 1928). It occurs in all resistive materials. For a photoconductor of resistance R_d, the Johnson noise mean square current it expressed as

$$\overline{i_J^2} = \frac{4kT\Delta f}{R_d}$$ [Dereniak, 1984]

where k is the Boltzmann constant, T is temperature, R_d is the detector resistance, and Δf is the electrical bandwidth [Dereniak, 1984].

3.5.2.3 Generation-Recombination Noise

The generation-recombination noise is caused by the fluctuation in generation rates, recombination rates, or trapping rates in the photoconductor thus causing fluctuations in free carrier current concentration. Two processes affect the fluctuation in rate of generation and recombination: thermal excitation of carriers and photon excitation. The expression for the combination of generation-recombination noise due to both photon and thermal excitation is

$$I_{G-R}^2 = 4q(q\eta\phi_B A_d G^2 + q g_{th} G^2) \qquad \text{[Dereniak, 1984]}$$

where q = electron charge
η = quantum efficiency
ϕ_B = photon irradiance
A_d = detector area
G = photonconductive gain
g_{th} = thermal generation rate

The second term in the above equation is the fluctuation in the rate due to the thermal generation of carriers in the photoconductor. If the devise is cooled sufficiently, thermal generation will decrease, so that it can be neglected. Therefore, when determining generation-recombination noise, most references use the photon noise that dominates the noise for cooled detectors. The expression for photon noise normally used is:

$$\overline{i_{G-R}^2} = 4q^2 G^2 \eta Q_p A_d \qquad \text{[Dereniak, 1984]}$$

3.5.2.4 Summation of Noise Sources

Figure 14 showed the dominant noise in various frequency regions. The noises add in quadature (variances add). Therefore, for any frequency region in Figure 14, the noise is the summation of all the noise and expressed as

$$\overline{i_{nt}^2} = \overline{i_{1/f}^2} + \overline{i_J^2} + \overline{i_{G-R}^2}$$

and one of the terms represents the dominate noise

$$\overline{i_{nt}^2} = \left[\frac{B_1 I^2 \Delta f}{f^{\beta}} + \frac{4kT\Delta f}{R_d} + 4q^2 G^2 \eta Q_p A_d \Delta f \right]$$ [Dereniak, 1984]

3.5.3 Background Limited Performance

In coherent optical radiation has a fundamental and unavoidable built-in noise term that is due to the random rate of generation of photons that results in a random rate of arrival of these photons. Mathematical analysis of the Poisson statistics governing this random emission of photons shows that the uncertainty in the number of photons collected in any time interval is about equal to the square root of the magnitude of the number of photons collected in any time interval [Marquis, 2003]. This process is known as *BLIP* or **B**ackground **LI**mited **P**erformance. Photovoltaic D*BLIP is expressed as

$$D^*_{\lambda}(BLIP)_{PV} = \frac{\lambda}{2hc}\left(\frac{\eta_Q}{Q_B}\right)^{1/2}$$ [Marquis, 2003]

Where Q_B is the total photon flux impinging on the detector in photons/second, also known as background irradiance.

3.5.4 Detector Performance

The following example illustrates the use of the figures of merits in determining the performance of a given detector. This example is presented in Dereniak, 1984. A typical test configuration for measuring detector performance with a blackbody source is shown in Figure 16. The blackbody source is usually 500 K for a thermal infrared detector test, and 2870 K is used for visible and near infrared detectors. The variable-speed chopper modulates the signal frequency f by rotating a notched wheel in front of the source. The notches alternately cover and uncover the source producing a nearly square-wave signal if the source aperture is small compared to the notch width.

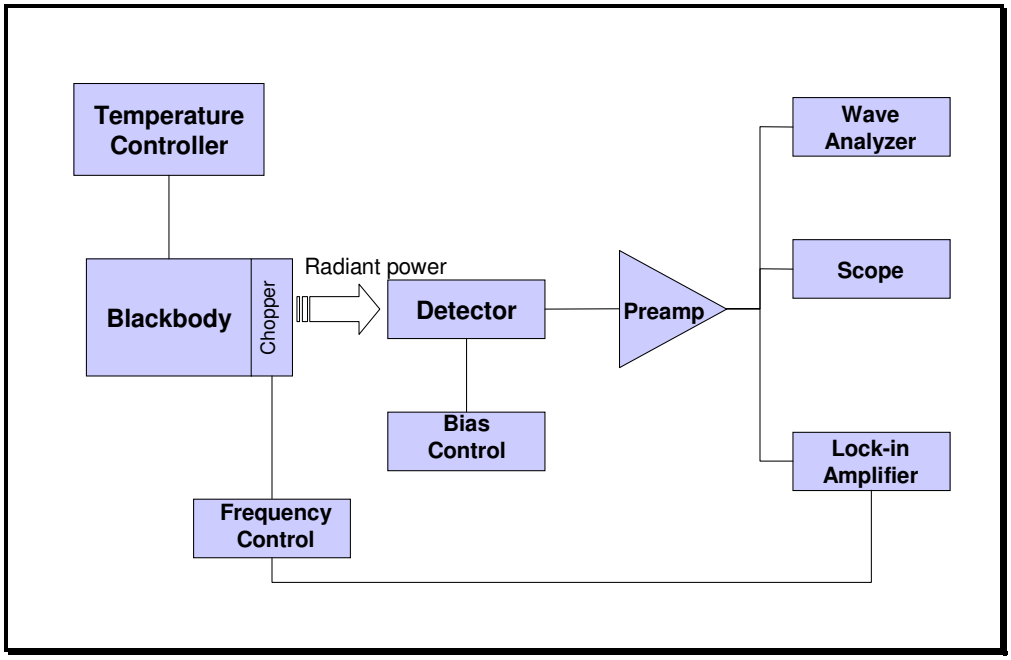

Figure 16. Blackbody Detector Testing Configuration

The detector is located at a known distance from the sources so that the signal on the detector can be calculated. The detector bias for the optimal signal-to-noise ratio must be found experimentally for each individual detector. An amplifier of known gain, noise level, and frequency is used to provide the signal level required by the wave analyzer. The wave analyzer is an rms voltmeter that has a turntable bandpass filter set to a center frequency f with bandwidth Δf. A lock-in voltmeter is often used in place of the wave analyzer and provides synchronous detection of the electrical signal at frequency f. The known data required to specify the performance of an infrared photodetector is given in Table 3.

Table 3. Sample Data For IR Photoconductor

								Blackbody Source		
Room Temperature (K)	Bias (V)	Signal (mV)	Noise (μV)	Δf (Hz)	f (Hz)	A_d (mm^2)	Detector FOV	Range (m)	Temperature (K)	Diameter of Aperture (cm)
300	90	30	30	10	1000	1	20^o	2.5	500	1

The rms signal incident on the detector is calculated by:

$$\phi_e^S = \frac{L_e^S A_{BB} A_d}{R^2} \tau F_F$$

where L^S_e is the signal radiance, A_{BB} is the area of the blackbody source aperture, A_d is the detector area, R is the separation between the source and the detector, τ is the transmission of the intervening atmosphere and optical windows, and F_F is the form factor peak-to-peak signal to rms signal. The rms radiant signal must be calculated because the resulting electrical signal from the detector is measured by an rms voltmeter. The signal radiance is given by:

$$L^S_e = \frac{\varepsilon_{BB}\sigma_e T^4_{BB}}{\pi} - \frac{\varepsilon_{rm}\sigma_e T_{rm}}{\pi}$$

where ε_{BB} is the emissivity of the source T_{BB} is the temperature of the source, ε_{rm} is the weighted average emissivity of the chopper wheel and room environment in the detector field of view, and T_{rm} is the room and chopper temperature. Assuming

$\varepsilon_{BB}=\varepsilon_{rm}=1$

T_{BB} = 500 K

T_{rm} = 300 K

L^S_e is calculated to be 0.1 W cm^{-2}sr^{-1} (watts per square centimeter per steradian).

The value of F_F can be found by adding the normalized rms values of all Fourier components of the signal waveform in quadature. For this case, with the given data, clearly only the fundamental sine wave at 1000 Hz is passed by a filter of bandwidth 10 Hz. The second harmonic of 2000 Hz and all higher order Fourier components are suppressed by the narrow filter. When the source is much smaller than the chopper blade width, the wave form is a square wave for equal blade and gap width (50% duty cycle). The square wave expressed as a Fourier series is:

$$A(t) = \frac{4A_o}{\pi}\sum_{n=1}^{\infty}\frac{1}{2n-1}\sin\left[(2n-1)\omega t\right]$$

where A_0 is the peak amplitude $\omega=2\pi f$, and t is time. The fundamental term is

$$A(t) = \frac{4A_0}{\pi}\sin\omega t$$

The rms value is

$$a = \left[\frac{16A_0^2}{\pi^2 T} \int_0^T \sin^2 \omega t dt \right]^{1/2}$$

where $T=1/f$ is the period. Then the equation above can be written as

$$a = \frac{4A_0}{\pi\sqrt{2}} = 0.9A_0 = 0.45(2A_0)$$

where $2A_0$ is the peak-to-peak amplitude, and 0.45 = F_F in this case. The value of F_F for the entire square-wave series (wide bandwidth Δf) is 0.707. When the source aperture is equal to the chopper blade spacing with 50% duty cycle, the signal waveform is triangular. The Fourier series expansion is:

$$A(t) = \frac{8A_0}{\pi^2} \sum_{n=1}^{\infty} \frac{(-1)^{n+1}}{(2n-1)^2} \sin[(2n-1)\omega t]$$

and the fundamental is

$$A(t) = \frac{8A_0}{\pi^2} \sin \omega t$$

The rms value is

$$a = \frac{8A_0}{\pi^2\sqrt{2}} = 0.572A_0 = 0.286(2A_0)$$

It is standard practice to test detectors using a sufficiently narrow bandwidth that only the fundamental term of the signal waveform is measured. The values of F_F therefore range between 0.286 and 0.45. Normal practice produces a signal waveform that is nearly square. Therefore, F_F=0.45 is used to continue this example calculation. The performance of the photoconductor can now be calculated from the data in Table X. Assuming τ = 0.9 and F_F = 0.45 the rms signal on the detector is

$$\phi_e^S = \frac{L_e^S A_{BB} A_d}{R^2} \tau F_F = \frac{(0.1)(\pi 0.5^2)(.01)}{250^2}(0.9)(0.45) = 5\times10^{-9} W$$

This power is spread across the entire blackbody spectrum and the detector, which is characterized by a cutoff wavelength, does not respond to all of this power. By the definition of blackbody responsivity, however,

$$\Re_V(500K,1000Hz) = \frac{30\times10^{-3}V}{5\times10^{-9}W} = 6\times10^{6}V/W$$

The blackbody NEP is

$$NEP(500K,1000HZ) = \frac{\phi_e^S}{S/N} = \frac{5\times10^{-9}W}{\left(30\times10^{-3}/30\times10^{-6}\right)} = 5\times10^{-12}W$$

The blackbody D* is

$$D^*(500K,1000Hz) = \frac{\sqrt{A_d\Delta f}}{NEP(500K,1000Hz)} = \frac{\left(10^{-2}cm^2\right)(10Hz)}{5\times10^{-12}W}$$

$$= 6.3\times10^{10}cm\cdot Hz^{1/2}\cdot W^{-1}$$

An infrared photoconductor that achieves this level of performance must be cooled well below room temperature of 300 K. This fact provides the opportunity to test experimentally whether or not the detector is background limited. A spherical mirror of low emissivity can be placed such that the detector is at the center of curvature. Then only the cold detector itself contributes to the background, except for a very small contribution from the mirror for which $\varepsilon < 0.03$ is commonly achieved. If the noise output is significantly reduced when the mirror blocks out the background, then the detector is operating in a background noise-limited condition. The relation between blackbody D^*_{BLIP} and peak spectral D^*_{BLIP} can then be used to calculate the peak spectral figures of merit. The peak spectral D^*_{BLIP} is calculated from

$$D^*_{BLIP}(\lambda_p, f) = K(T, \lambda)D^*_{BLIP}(T_{BB}, f)$$

The quantity K(T, l) is the ratio of the BLIP peak spectral D* to the BLIP blackbody D* and can be calculated for various temperatures across peak cutoff wavelengths. Values of K(T, l) are contained in Blackbody Detectivity tables in some texts (see Appendix C, Dereniak, 1984). From this data we obtain:

$$D^*(14\mu m,1000Hz) = 2.3(6.3\times10^{10}) = 1.45\times10^{11}cm\cdot Hz^{1/2}\cdot W^{-1}$$

Quantum efficiency is calculated from:

$$\eta(\lambda_p, f) = \left[D^*_{BLIP}(\lambda_p, f)\frac{hc\sin\theta_{1/2}}{\lambda_p}\right]^2 \times 2\int_0^{\lambda_p} M_p(\lambda,T)d\lambda$$

Assuming a 20° field of view and T_B = 300 K, we obtain

$\eta(14\ \mu m, 1000\ Hz) = 0.077$

The figures of merit at other than peak response wavelengths can be found if the spectral response rate is known. The spectral D* relates to the spectral voltage responsivity in the equation:

$$D^*(\lambda, f) = \frac{\sqrt{A_d \Delta f}}{V_{rms}} \Re_V(\lambda, f)$$

The response of the detector under test is ratioed to the calibrated, spectrally flat response of a reference standard thermal detector. The thermal detector will be slower in many cases than the detector under test. This limits the chopping frequency *f* to low values. The monochromator is an optical devise that selects a desired narrow wavelength band of center wavelength λ and width $\Delta\lambda$. The resulting plot displays the spectral responsivity of the detector under test normalized to the responsivity of the reference detector. The spectral response of the detector must be measured if the detector is not BLIP, or if the precise spectral characteristics of the detector at other than the response peak must be known.

CHAPTER IV
INFRARED SENSOR DESIGN

4.1 System Architecture

Figure 17 depicts a basis IR sensor design, and presents the major component of the system. The previous chapter described the process of detecting the photon, from emission, to its travel through the atmosphere, through the optics, and onto the detector. This chapter will describe the many components of the senor that transforms the photon into information visible to the observer. Each of these major components, the optics, the detector (and dewar), the cooler, the readout, and the display are significantly complex systems by themselves. Each component is made up of multiple technologies and requires the collaboration of multiple engineering disciples in the design.

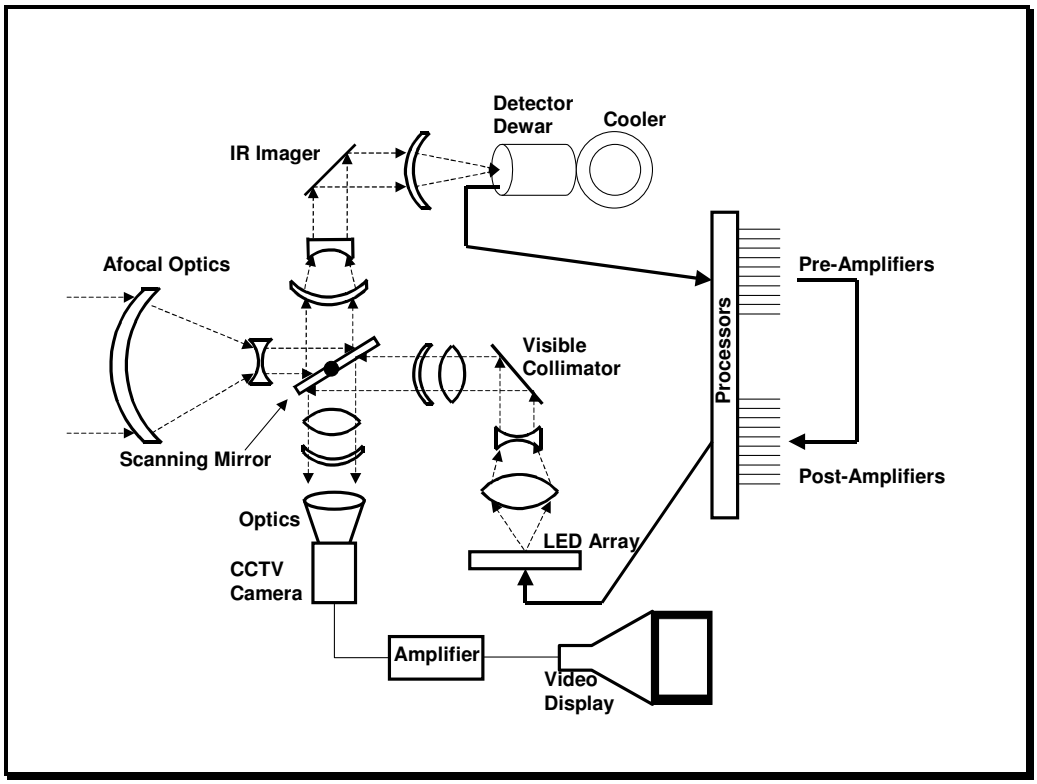

Figure 17. Basic IR System Design

It is hoped that the reader at this point begins to appreciate the vast amount of knowledge necessary to design such a system, and realize this report can only scratch the surface. The reader should also realize the important role of the system engineer in the design process of the IR sensor system. The technologists, scientists, and engineers can design any of the components depicted in the figure to achieve almost any performance criteria. But there are always design limitations, such as weight, power consumption, size (volume), memory utilization, and throughput. There are also programmatic limitations, most importantly time and money. It is the system engineer that brings the engineers, technology, and components together to meet the objectives that are often diametrically opposed. Several of the design trade offs are described in this section. The "best" component, based on performance, may not always be the right choice for the system. The component that meets the weight and size requirements, with the *required* performance is the desired choice.

4.2 Component Materials

This section investigates the major components that comprise the IR sensor system. Common materials are described in terms of performance parameters and considerations for that component. Except where otherwise noted, the vast majority of Section 4.2 comes from The Infrared and Electro-Optical Systems Handbook, Volume 3 Electro-Optical Components [Rogatto, 1993]. This is an excellent reference for comparing materials and component characteristics.

4.2.1 Optical Materials

This section describes the key characteristics of the lenses and structural materials. Common materials used for lenses are Germanium, Zinc Sulfide, Zinc Selenide, Silicon, Gallium Arsenide, and TI 1173. Common housing and structural materials include Aluminum, Magnesium, Stainless Steel, Titanium, and Berylluim.

4.2.1.1 Refractive Index

The refractive index is the ratio of the velocity of light in a vacuum to that in a medium. Ideally the refractive index of the thermal imaging lens should be high. A higher refractive index results in a shorter focal length, requires less curvature and thickness, and fewer lens elements. Thus, a high refractive index results in a more compact system design. The refractive index should not change with temperature (Thermal Dispersion), and be constant over the desired wave band (Optical Dispersion). Low optical dispersion is necessary to minimize chromatic aberration. Table 4 [Lloyd, 1975] shows the refractive indices over several wavelengths and the change in the refractive index with change in temperature ($\delta n/\delta T$) of the common lens materials [Lloyd, 1975; Marquis 2003].

Table 4. Refractive Indicies

Material	Useful IR Waveband (μm)	Refractive Indices (n)									δn/δT @ 300 K (10^{-6} °C^{-1})
		n(3μm)	n(4μm)	n(5μm)	n(8μm)	n(9μm)	n(10μm)	n(11μm)	n(12μm)	δn(μm)	
Germanium	2 - 23	4.049	4.0244	4.0151	4.0053	4.004	4.0032	4.0026	4.0023	0.0467	280 to 300
Silicon	1.5 - 15	3.4324	3.4254	3.4221	3.4184	3.418	3.4177	3.4177		0.0147	162 to 168
Zinc Sulfide	0.4 - 14.5	2.2558	2.2504	2.2447	2.2213	2.2107	2.1986	2.1846	2.1689	0.0869	
Zinc Selenide	0.5 - 22	2.44	2.435	2.432	2.418	2.413	2.407	2.401	2.394	0.046	100
Gallium Arsenide	0.9 - 11				3.34		3.1			0.24	149
TI 1173	1 - 14	2.6263	2.62	2.6165	2.6076	2.604	2.6	2.596	2.592	0.0343	80

4.2.1.2 Strength and Hardness

Mechanical strength is required to resist shock, vibration, impact, aerodynamic pressure and deforming forces. Strength is normally defined in terms of stress and strain. The force is measured as pressure, or a force per unit area. If the force is normal to the body, the stress is dilational or compressional. If the force is parallel to a surface, the stress is a shear. A dilational strain can be the change in length divided by the mean or the original length. A shear is the difference in displacement of two parallel planes divided by the distance between them. Young's modulus E is the tensile stress divided by the linear strain. Hardness describes the ability of the material to resist scratching and abrasion. Most methods of measuring hardness are based on pressing an indenter of a specially prescribed shape into the material. The measure is a description of the area or length of the indentation. Usually, and sometimes necessarily, the load on the indenter is specified. Three types are Vickers, Brinnell, and

Knoop indenters. The Vickers hardness is the load in kilograms divided by the area of indentation made by a pyramidal indenter that has an angle of 136 degrees between opposite faces and 146 degrees between opposite edges. Brinnell hardness is the load in kilograms divided by the curved area made by a spherical indenter. Knoop values are obtained with an indenter almost identical to the Vickers indenter. The area is usually in square millimeters. Some measurements vary with the applied load [Rogatto, 1993]. Table 5 [Lloyd, 1975] shows the Young's Modulus for lens and housing material, and Knoop hardness index of the common lens material.

Table 5. Strength and Hardness

Lens Material	Young's Modulus (10^6 psi)	Knoop Hardness (kg/mm^2)
Germanium	15	692 - 850
Silicon	19	1150
Zinc Sulfide	14	250
Zinc Selenide	9.75	100
Gallium Arsenide	12	750
TI 1173	3.1	150
Housing Material		
Aluminum	10	
Magnesium	5.5	
Stainless Steel	28	
Titanium	16	
Berylluim	42	

4.2.1.3 Absorption

Low absorption and high dispersions allows for good transmittance of the optics and for efficient system design. Absorptivity or absorptance is the ratio of power lost to the material. The absorption coefficient is normally expressed in units of reciprocal centimeters (cm^{-1}) [Rogatto, 1993]. The absorption coefficient and dispersion index are shown for the common materials in Table 6 [Marquis, 2003].

Table 6. Absorption Coefficient and Dispersion Index

Material	Absorption Coefficient @ 10 μm (α, cm^{-1})	Dispersion Index @ 8 to 10 μm
Germanium	0.02	1000
Silicon		3454
Zinc Sulfide	0.11	30
Zinc Selenide	0.003	80
Gallium Arsenide	0.02	
TI 1173	0.06	140

4.2.1.4 Thermal Expansion

Thermal expansion is a measure of the change in a material's dimensions as a result of a change in temperature. Most thermal imaging refractive lens materials, including Germanium, have refractive indices that change significantly with temperature. Many application of thermal imaging systems used in temperature extremes of –20° C to 40° C are not uncommon. In other applications such as high altitude aircraft, high-speed aircraft, or space vehicles, the extremes may be greater. Thus the effects on lens parameters due to thermal index changes cannot be ignored. The change in dimensions caused by the change in temperature will cause defocus of the imaging system. Lens housings also expand and contract to produce defocus [Lloyd, 1975]. In designing the system, it is important that the expansion coefficients of both the lens and the housing material are comparable so that the materials expand and contract together. If not, not only will it result in defocus, but also additional stresses are introduced. Table 7 [Marquis, 2003] contains the expansion coefficients of common lens and housing materials.

Table 7. Thermal Expansion Coefficients

Lens Material	Expansion Coefficient @ 300 K (10^{-6} K^{-1})	Housing Material	Expansion Coefficient @ 300 K (10^{-6} K^{-1})
Germanium	6	Aluminum	16.3
Silicon		Magnesium	16 - 19
Zinc Sulfide	7	Stainless Steel	11.5
Zinc Selenide	8	Titanium	6.6
Gallium Arsenide	6	Berylluim	6.4
TI 1173	15		

4.2.1.5 Summary

No known material possesses all of these desirable characteristics, but the ones described in this section come the closest. Part of the IR system design is the tradeoff between material capabilities and performance requirements. The properties of Germanium and Silicon are overall more desirable. That is why these materials have emerged as standards for IR optics. Figure 18 shows a Silicon lens (a) and a Germanium lens (b) from the Thorlabs, Inc. online catalog [Thorlabs, 2006]. The silicon lens is a plano/convex lens designed for the 1.2 to 8.0 μm wavelength range with an index of refraction of 3.425 at 4.0 μm. The germanium lens is a plano/convex lens designed for the 2.0 to 16.0 μm wavelength range with an index of refraction of 4.004 at 10.0 μm.

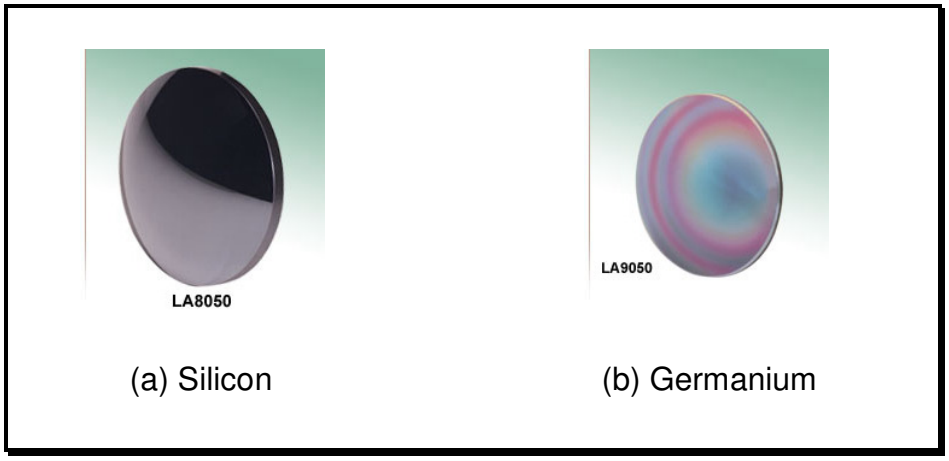

Figure 18. Silicon and Germanium Lenses

4.2.2 Detectors

As discussed in Chapter 2, infrared detectors have been the technology-pacing item for electro-optic systems. The development of new detector materials and fabrication processes has enabled the growth over the last few decades. This section describes some of the more common materials currently in use. Figure 19, from Raytheon Vision Systems, is an example of how the different detector materials are used for different IR applications.

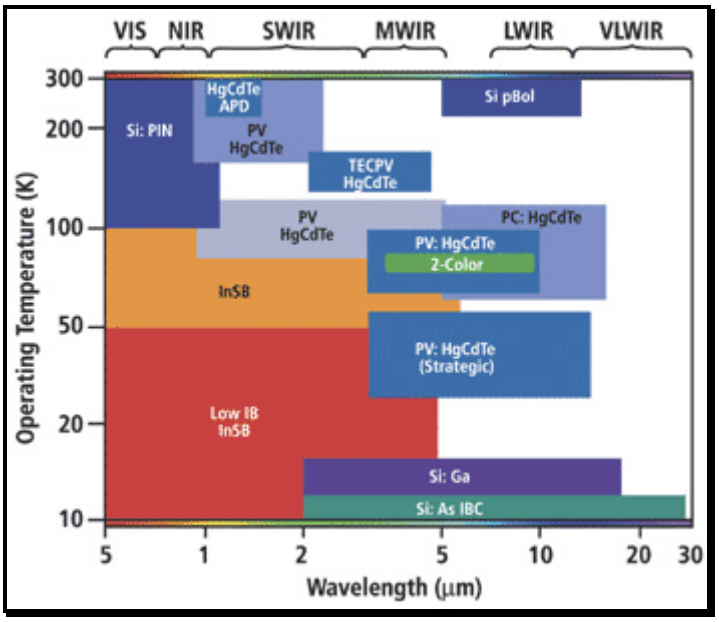

Figure 19. Detector Materials for IR Applications

4.2.2.1 Mercury Cadmium Telluride (HgCdTe)

HgCdTe detectors are available to cover the spectral range from 1 to 25 μm. The versatility of HgCdTe detector material is directly related to being able to grow a broad range of alloy compositions in order to optimize the response at a particular wavelength. For applications at 80 K, photovoltaic (PV) HgCdTe is generally limited to wavelengths of approximately 12 μm or less in order to maintain a high enough impedance to interface with on-focal-plane complementary metal-oxide semiconductor (CMOS) readouts. For MWIR applications with spectral cutoffs of 3 to 4.7 μm, operation is possible at temperatures in the range of 175 to 220 K, which can be achieved with thermoelectric cooling. SWIR applications can operate at correspondingly higher temperatures, up to and above room temperature. PV HgCdTe arrays have been made in linear with 240, 288, 480, and 960 elements, 2-D scanning arrays with TDI, and 2-D staring formats from 32 X 32 up to 480 X 640. Pixel sizes ranging from 20 μm^2 to more that 1 mm have been demonstrated. These devices have applications for push-broom scanning systems for Landsat earth resource mapping as well as thermal imaging and search and track applications in the SWIR, MWIR and LWIR regions.

PV HgCdTe laser detectors, specialized for use with CO_2 lasers at 10.6 μm and 80 K operation, are available with response speeds up to 1 GHz and higher. Performance is commonly measured in the heterodyne mode where the CO_2 laser provides the local oscillator frequency. Detector performance can be compared with the quantum efficiency limit for a heterodyne receiver under the conditions in Table 8 [Rogatto, 1993]. Experimental heterodyne quantum efficiencies exceed 50% at frequencies less than 500 MHz, and are approximately 30% at higher frequencies. These detectors are useful for laser radar imagery and can be made as single elements or in small arrays.

Table 8. Typical Performance Specification for an LWIR PV HgCdTe Array

Array Format	240 X 4
Pixel Size	40 X 40 μm
Spectral Response Cutoff	$10.0 < \lambda < 10.5$ μm
Average D* at 77K and 30^o FOV	$> 1.2 \times 10^{11}$ Jones
D* Standard Deviation	< 15%
D* Defects below 0.6×10^{11} Jones	< 4 pixels
Quantum Efficiency (without antireflection coating)	> 65%

Photoconductive (PC) HgCdTe technology is limited at present time to linear arrays, although custom 2-D arrays up to 10 X 10 have been made for unique applications. Production products include 12 μm cutoff arrays of 30, 60, 120, 160, and 180 elements for operation at 80 K as well as 5 μm cutoff arrays of 30 elements for operation at 190 K. In all the PC HgCdTe linear array configurations, the signal from each detector is brought outside the dewar for preamplification and multiplexing. The development of on-focal-plane multiplexing technologies capable of handling the low impedance of photoconductive devices has not yet been demonstrated. A significant improvement in the gain of PC devices has been realized in the past decade with the development of trapping-node detectors and detectors with blocking contacts. The improved gain can be used to either reduce bias power and/or raise the detector noise levels so that preamplifier noise is less critical in the imaging system electronics. A further benefit of the improved gain is that 1/f noise is significantly reduced. The 1/f noise "knees", in which the 1/f

component is equal to the generation-recombination noise level (see Figure 15), are typically 1000 Hz in ordinary PC HgCdTe devices, but only of the order of a few hundred hertz or less in higher-gain counterparts at 80 K and for f/2 background flux conditions [Rogatto, 1993].

4.2.2.2 Platinum Silicide (PtSi)

PtSi detectors are the largest IR image sensor formats available. The combination of large array formats and excellent array responsivity uniformly makes PtSi attractive for a variety of high-background-flux applications. The spectral response or quantum efficiency of PtSi detectors is unusual and related to the photodetection mechanism. Infrared photons energize electrons for the PtSi layer, which then have a probability of tunneling through the PtSi Schottky barrier. Since the tunneling probability is an exponential function of the photon energy, the quantum efficiency decays exponentially with wavelength before falling off more steeply as the cutoff threshold is approached on a per photon scale. As a consequence, quantum efficiency is quite low for PtSi on the 4 to 5 μm spectral region, typically of the order of 0.1% to 1%. Imagery is nevertheless very good under high-background conditions due to the large number of pixels available, combined with the excellent operability and uniformity of PtSi. Responsivity uniformity one-sigma values as low as 0.2% have been reported. A number of PtSi camera systems are available commercially. Specifications for typical PtSi imaging arrays are summarized in Table 9 [Rogatto, 1993].

Table 9. Typical Performance of Hybrid PtSi Arrays at 77 K

	Configurations	
	256 X 256	488 X 640
Elements	65,536	312,320
Spacing (μm)	30	20
Fill Factor (%)	> 88	> 80
Emission Factor	> 0.3	> 0.3
Responsivity (mV/K at f/2, 60 fps)	> 10	> 10
Operability	> 96	> 96
Dynamic Range (dB)	64	64
Noise Floor (electrons)	< 200	< 200
Frame Rate (frames/s)	60	60
NEΔT (^{o}C at f/2)	< 0.09	< 0.09

4.2.2.3 Indium Antimonide (InSb)

Photovoltaic InSb remains popular detector for the MWIR spectral band at 80 K. InSb material is highly uniform and, combined with planar-implanted process in which the device geometry is precisely controlled, the resulting detector array responsivity uniformity is good to excellent. Starring arrays of backside-illuminated, directed hybrid InSb detectors in formats up to 640 X 480 are available with readouts suitable for high-background f/2 operation and for low-background astronomy applications as well. Specifications for astronomy array devices are summarized in Table 10 [Rogatto, 1993]. Linear array formats of 64 and 128 elements are produced with frontside-illuminated detectors for both high-background and astronomy applications as well. Linear and 2-D arrays based on charge injection devices have also been developed in InSb. Since the spectral response of InSb shifts to longer wavelengths as the temperature increases, thermally generated noise increases rapidly with higher operating temperature for InSb devices. Nevertheless, operation up to at least 145 K is possible at high-background-flux levels, making these devices useful for satellite applications such as Landsat, which rely on radiative coolers [Rogatto, 1993].

Table 10. Typical Performance of InSb Astronomy Arrys

50 K , Background Flux $< 10^9$ photons/cm^2 s^{-1}	Configurations	
	58 X 62	256 X 256
Elements	3,596	65,536
Spacing (μm)	76	20
Fill Factor (%)	> 90	> 90
Peak Quantum Efficiency (%)	> 90	> 90
Dark Current (fA)	< 2.5	< 1
NEP (aW) @ 3 μm, 100 s	< 10	
NEP (aW) @ 2.2 μm, 1s		< 20
Operability (%)	> 96	> 96
Integration Capacity (q)	10^6	5 x 10^5
Mean Readout Noise (q) @ 260-ms integration	< 400	
Mean Readout Noise (q) @ 1-s integration		< 75

4.2.2.4 Extrinsic Silicon (Si) Detectors

Extrinsic silicon detectors rely on photoexcitation of impurity levels within the bandgap. The spectral response of the detector depends on the energy level of particular impurity state and the density of states as a function of energy in the band to which the bound charge carrier is excited. Table 11 [Rogatto, 1993] lists some of the common impurity levels and the corresponding long-wavelength cutoff. The exact long-wavelength spectral cutoff is a function of the impurity doping density, with higher density giving slightly longer spectral response.

Table 11. Common Impurity Levels Used in Extrinsic Si IR Detectors

Impurity	Energy (meV)	Cutoff (mm)	Temp (K)
Indium	155	8	40 - 60
Bismuth	69	18	20 - 30
Gallium	65	19	20 - 30
Arsenic	54	23	13
Antimony	39	32	10

The performance of extrinsic silicon detectors is generally background limited with quantum efficiency that varies with the specific dopant and dopant concentration, wavelength, and device thickness. Typical quantum efficiencies are in the range of 10% to 50% at the response peak. Extrinsic silicon detectors are frequently cooled with liquid He for applications such as ground- and spaced-based astronomy. Closed-cycle two- and three-stage refrigerators are available for use with these detectors for cooling to 20 to 60 and 10 to 20 K, respectively. Extrinsic silicon detectors have been made in 58 X 62 element formats for low-background astronomy applications. Table 12 [Rogatto, 1993] lists the specifications of Ga-doped detectors in this format. Other impurity dopants such as Sb or As can be substituted for Ga. Both linear scanning and 2-D arrays can be readily produced. Linear arrays more than 2.5 cm in length have been demonstrated [Rogatto, 1993].

Table 12. Typical Performance of Si:Ga Astronomy Arrays

4 K , Background Flux < 10^9 photons/cm^2 s^{-1}	Configuration
	58 X 62
Elements	3,596
Spacing (μm)	76
Fill Factor (%)	> 90
Peak Responsivity (A/W)	> 1
Dark Current (fA)	< 0.1
NEP (aW) @ 15 μm, 1 s	< 40
Operability (%)	> 98
Integration Capacity (q)	~2 x 10^6
Mean Readout Noise (q)	< 300

4.2.2.5 Lead Sulfide (PbS) and Lead Selenide (PbSe)

Lead Sulfide (PbS) and Lead Selenide (PbSe) detector materials may be chemically deposited as polycrystalline thin films on insulated substrates. Both are employed as photoconductors and can operate at any temperature between 300 and 77 K. The responsivity uniformity of PbS and PbSe is generally of the order of 3% to 10%. When sufficiently cooled to eliminate thermal noise, the D* performance of PbS and PbSe at high-background-flux levels comes within about a factor of 2 of the background limit, implying a quantum efficiency of about 30%. Quantum efficiency is probably limited by incomplete absorption of the incident flux in the relatively thin (1 to 2 μm) detector material deposited by the chemical process. PbS and PbSe arrays have been made in a variety of linear array formats for use in focal planes not having cooled readouts. Operability of 99% to 100% is readily achieved for these arrays having 100 or fewer elements. Large arrays of between 1000 and 2000 elements on a single substrate have also been produced with operability exceeding 98%. The high impedance of PbS and PbSe photoconductive devices allows them to be interfaced with CMOS readout circuits. Linear array formats with CMOS readouts are available in 64, 128, and 256 element configurations. Table 13 [Rogatto, 1993] summarizes the performance of PbSe arrays in these configurations. PbSe has significant 1/f noise, with a knee frequency of the order of 300 Hz at 77 K, 750 Hz at 200 K, and 7 kHz at 300 K. This generally limits this material to use in scanning imagers [Rogatto, 1993].

Table 13. Typical Performance of PbSe Linear Array with CMOS Multiplexed Readout

Configuration 64, 128, 256 Linear	
Pixel Size (μm)	38 X 56
Spacing (μm)	51
D* (peak, 1400 Hz) (Jones)	> 3 x 10^{10}
Operability (%)	> 98
Dynamic Range	2000
Uniformity	< 20%

4.2.2.6 Summary

Selection of detector type and material is dependant on performance requirements, such as response time, sensitivity to detection (D*), IR spectral range, and reliability. These parameters are summarized in Table 14 [Jha, 2000] for some of the materials covered in this section. It is important to note that higher sensitivity and wider spectral bandwidth are possible in lower cryogenic operations. HgCdTe detectors offer satisfactory performance at lower cost. However, any substrate impurity will lower detector yield, sensitivity, and reliability [Jha, 2000].

Table 14. Detector Material Performance Parameters

Detector Material	Response Time (ns)	Detectivity (D*) (cm $Hz^{-1/2}$/W)	IR Range (μ)	Percent of Energy @ 350 K
PbS	100K - 500K	2 x 10^{11} @ 300 K	1.80 - 2.37	0.2
InSb	800	10^{11} @ 77 K	3.0 - 3.5	5.3
Ge:Cu	50	2 x 10^{10} @ 5 K	8 - 25	65
HgCdTe	100	5 x 10^{10} @ 77 K	8 - 14	39

Figure 20 shows a PbS Focal Plane Array from Northrop Grumman [Northrop, 2006]. The M2105-256-2D detector is a linear 256-element array designed for a spectral range of 1 to 3 μm, with a detectivity (D*) of 2 X 10^{11} to 3 X10^{11}, and a responsivity of 5 X 10^{7} to 1 X 10^{8}.

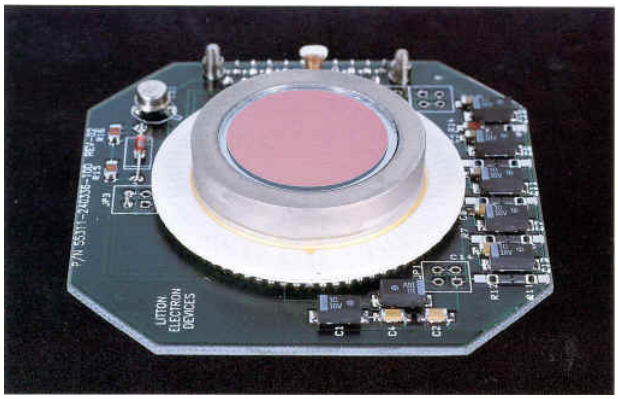

Figure 20. PbS Focal Plane Array

4.2.3 Readout Electronics

The readout integrated circuit (ROIC) is a highly integrated set of focal plane electronic functions combined into a single semiconductor chip. Its primary function is to provide infrared detector signal conversion and amplification, along with time multiplexing of data from many detectors to just a minimum number of outputs. ROICs can contain tens to hundreds of thousands of individual unit cells, each with critical detector amplifiers and multiplexer switches that are normally processed using conventional silicon integrated circuit technology. They are most often implemented in complementary metal oxide semiconductor (CMOS) technology, allowing higher resolution and greater sensitivity. The ROIC functions include preamplifier, signal processor, multiplexer, and video amplifier. Figure 21 [ORNL, 2003] is an example of readout electronics board assembly. This Application Specific Integrated Circuit (ASIC), developed by Oak Ridge National Laboratory (Department of Energy), is an example of low power, low cost design for sensor systems.

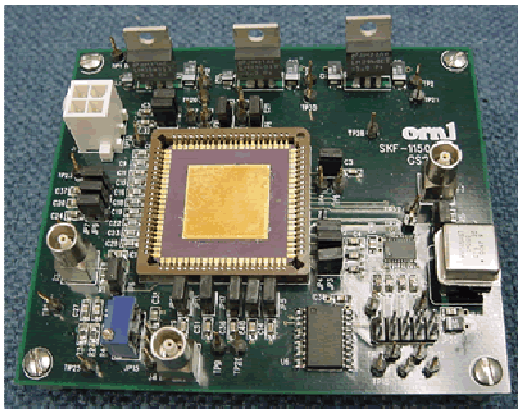

Figure 21. ASIC Readout Electronics Board

4.2.3.1 MOSFET Primer

Although discrete preamplifiers can be designed with bipolar junction transistor (BJT) or junction field effect transistor (JFET) technology, integrated circuit forms of the preamplifier are most commonly fabricated in silicon CMOS technology because of the operating temperature range, power and noise characteristics of the metal oxide semiconductor FET (MOSFET). Silicon CMOS devices can be designed to operate from room temperature to below 10 K. A *N*-channel MOSFET is comprised of *n*-implanted drain and source regions isolated from each other by the *p*-doped silicon substrate, or *P*-well. A gate, usually composed of polysilicon, lies above a thin dielectric layer (usually SiO_2) on the semiconductor surface between the two diffusions. In the simplest transistor action, a positive gate-to-source voltage V_{gs} induces a field in the surface region of the semiconductor. If the gate voltage is above a specific threshold V_t, the resulting field repels majority mobile carriers (holes) and attracts electrons, forming a very thin inversion region, or *n*-channel, at the surface of the semiconductor. The *n*-channel then provides a current path between the source and drain. The *P*-channel MOSFET is the same as the *N*-channel device but it utilizes opposite doping and voltages. Although most modern ROICs are comprised of MOSFETs and other components formed in CMOS integrated circuit technology, MOSFETs are not always the best choice for low noise amplification of detector signals. There is a strong relationship between detector impedance and optimum readout technology. Although the silicon MOSFET covers most infrared applications, it is not well suited for all detectors. Specifically, discrete readout

preamplifier implementations, popular in systems with few detector elements, can benefit from BJT, JFET, or MOSFET technology [Rogatto, 1993].

4.2.3.2 ROIC Performance Drivers

Sensor electronic designs, whether discrete or ROIC, are guided by requirements traceable to system performance parameters or input/output interface requirements. Key ROIC requirements are matched with respect to key system or interface requirements in Table 15 [Rogatto, 1993]. The signal-to-noise ratio (SNR) is the prime design driver in most sensor systems. To achieve SNR objectives, trade-offs must often be made between detector temperature, circuit area and power. Other important drivers include dynamic range, linearity, and operability. All requirements are interrelated and can be usually met given great enough real estate (detector size), power, and low detector temperature. These conventions are rarely allowed, resulting in designs requiring many trade offs and compromises between parameters. The designer should develop a dialog with the sensor user so that the evolving design accurately reflects the users needs [Rogatto, 1993].

Table 15. Key Readout Requirements and Systems performance and Interface Issues

Major Readout Performance Parameters	Related System Parameter or Interface Impact	Comments
NEC (noise equivalent charge)	Sensitivity	Minimized to enhance SNR
Power dissipation	Cooldown Time Life Weight	Limited cryogen/cooler life Cryogen weight/cooler size
Dynamic Range	Maximum saturation signal	Loss of signal
Crosstalk	System MTF (resolution) Blooming of saturated elements	Element to element
Frequency Response	System MTF (resolution) Latent images	Often related to crosstalk
Input Impedance	Signal linearity Noise	Detector bias changes with signal Loss of optimum detector bias
Linearity Reliability	Calibration Instrument Life	Proper identification Confidence of success
Gain	Sensitivity	Signal amplified above system noise floor
Output video driver impedance	Sensitivity MTF	EMI from environment crosstalk between multiplexed elements

4.2.3.3 Signal Processing

Incorporation of signal processing on an ROIC is often desirable in order to reduce off-focal-plane electronics, reduce the data rate, or perform processing prior to sampling and multiplexing. These two areas where on-chip signal processing can occur are: 1) Within the unit cell itself and 2) in the multiplexer prior to the output video amplifier. The most common forms of ROIC signal processing are band limited (provided by all reset integrator preamplifiers), sample and hold, corrected double sampling, and time delay integration [Rogatto, 1993].

Sample and Hold. Simultaneous integration of all elements of the sensor is often required. The signal for simultaneous integration is accumulated over a given time period in a snapshot mode. To reset the detector and preamplifier to begin integration of the next frame, the signal from the previous frame must be sampled and stored temporally for sequential readout by the multiplexer. The most common form of this type of sample and hold is composed of a MOSFET sampling switch, a hold capacitor, and a unity gain buffer amplifier. A simple output MOSFET source follower and load serves as buffer amplifier prior to multiplexing. The sample and hold circuit resides in the unit cell, and therefore puts limitations on minimum cell size because ample area is required for the three transistors and capacitor [Rogatto, 1993].

Correlated Double Sampling. Drift and 1/f noise are often dominant noise contributors in readout preamplifiers. Therefore, it is often desirable to recalibrate, or re-zero the amplifier chain periodically in order to achieve lower noise and greater absolute accuracy. This is normally accomplished in reset integrators by re-zeroing the output of the preamplifier at the beginning of integration. The output signal is initially sampled across the clamp capacitor during the onset of photon integration (after the detector is reset). The action of the clamp switch and capacitor subtracts any initial voltage from the output waveform. Because the initial sample is made before significant photon charge integrates onto the capacitor, the final integrated photon signal swing is unaltered. However, any offset voltage or drift present at the beginning of integration is removed, or subtracted, from the final value. This process of sampling each pixel twice, once at the beginning of the frame and again at the end, and providing the

difference is called correlated double sampling (CDS). This process can be performed within the unit cell, or numerically off the focal plane in a digital processor [Rogatto, 1993].

Time Delay Integration. A simple scanning senor chip assembly (SCA) includes a single row of detector elements that scan a scene and multiplex the resulting signal to the output. To generate an entire scene, the array is canned from one side of the field of view to the other. Sensitivity is limited in a sensor of this type by the dwell time, or equivalent time that an element is looking at a specific point in the scene. To reduce flicker and provide reasonable scene refresh rates, this scene is typically scanned 30 to 100 times per second. The dwell time of a given element will tend to reduce if a short scan time, high scene resolution, or large field of view is required. Placing a second row of detectors next to the first row produces a second image of the scene that is displaced in time. The two images can be added (integrated), after the first is scene delayed, to double the signal level with only modest increase in noise of the two frames. By adding rows of time-delay elements and performing the time-delay integration (TDI), the SNR of a scanning system can be improved by $\sqrt{n}$, assuming the system is detector limited, where n is the number of elements or rows in TDI. The TDI function can be performed via a large array of storage capacitors. However, it is most commonly implemented using a charged couple device (CCD) [Rogatto, 1993].

4.2.3.4 Data Multiplexers

The multiplexer (MUX), in its simplest form, is a series of switches or transfer wells that sequentially transports sampled data from many pixel elements and encodes them onto a common bus. Signals from tens to hundreds of thousands of detector elements can be multiplexed through a video driver to a signal output pad on the readout. Two common forms of multiplexers are available to the readout designer:

1) CCDs, which utilize a series of sequentially enabled potential wells, or metal insulator semiconductor (MIS) capacitors, to transfer charge to a floating gate or diffusion.
2) A set of switches that is enabled sequentially to a common bus.

Staring arrays utilize two multiplexers, one for the column and one for the row MUX. The column multiplexer shifts data at low speed from each unit cell to the end of the column; the data are then further multiplexed, at high speed, with other elements of the same row from subsequent columns. The output is thus formatted with pixel one of the first row through the last pixel in the first row followed by the data from pixel one in the second row through the last pixel in the second row and so on. If the multiple outputs are utilized, data can be formatted to address quadrants or interlaced columns of the ROIC unit cells [Rogatto, 1993].

4.2.3.5 Output Video Amplifiers

The output video driver buffers the encoded signal string from the ROIC multiplexer off the focal plane, through the cryogenic and ambient interface cables, and finally to a set of warm electronics where any necessary signal conditioning is provided prior to digitization or display. The primary concern of the video driver is the cryogenic power dissipation required to provide adequate frequency response and dynamic range. The limits of video driver power can be determined by evaluating the extremes in driver circuit configurations and output load capacitance. At the lower limit, power can be calculated from the energy required to charge and discharge the load capacitor. The most common type of video driver for cooled focal planes is the source follower found in most MOSFET implementations. The primary advantages of this circuit are simplicity, relatively low power, and near unit gain. Also, this configuration implements a current source load off the focal plane to minimize focal plane cryogenic power [Rogatto, 1993].

4.2.4 Cooling Systems

As with the other components of an IR sensor, the cooling system is very complex and constitutes a system within itself, requiring extensive engineering and application of several disciplines, such as thermodynamics, mechanical engineering, software engineering, and electrical engineering. The focus for this section is on the system engineering design fundamentals of the cooling system and examples of common key components.

4.2.4.1 Design Fundamentals

It is essential for the cooling system to provide an appropriate low-temperature heat sink. The heat sink could be a depletable liquid or solid cryogen within the system, a refrigerator and an appropriate power or heat source, or a low-temperature radiator. The system must provide adequate isolation from a warm environment. Temperature differences of several hundred degrees often exist between the low-temperature heat sink and the surroundings, providing a large potential for overwhelming heat fluxes. There should be proper linkage between cooled instrument components and the heat sink. Focal plane arrays and other optical components must usually be maintained at steady temperatures within rather narrow limits. This often provides an immense challenge in thermal design. Electrical reliability is also an immense challenge. From an electrical point of view, wires running between the warm surroundings and cooled components inside the instrument should have maximum conductivity, maximum diameter, and minimum length and be well shielded to minimize voltage drops and signal distortion. From a thermal point of view, wires are heat paths into the cold world of the cryostat and should have minimum conductivity, minimum diameter and maximum length. Thus, there is a direct conflict in objectives and trade offs and compromise is a necessary part of the design decisions. Finally, the mechanical integrity of the entire system is necessary. The mechanical task is often in direct conflict with the thermal task described above. Cooled components usually must be precisely located and rigidly supported, often under harsh dynamic conditions such as a rocket ride into space. From a mechanical point of view, the support structure should be massive and strong to provide the necessary rigidity. From a thermal point of view, the support structure should be light with small cross-sectional areas to minimize parasitic heat transfer. Again, compromise is necessary to arrive at a satisfactory design [Rogatto, 1993].

4.2.4.2 Low Temperature Heat Sink

One of the key components of the IR sensor cooling system is the low temperature heat sink. Every known substance can be made to exist as a solid, liquid, or gas depending on the pressure and temperature at which it is exposed. Those substances that normally exist as a gas at room temperature and pressure are called cryogens if liquefied or solidified. The drivers in cryogen selection are usually

temperature, mission life, weight, volume and system cost. As listed above, there are three common methods of using cryogens to provide a low-temperature heat sink: depletion, radiation, and refrigeration. The use of cryogenic refrigerators has the advantage over expendable cryogens for applications of long-term service without replenishment. Operating temperature, cooling capacity, power requirements, mass, reliability, lifetime, and vibration control are important issues in refrigerator selection, particularly for applications in space-deployed surveillance systems. Cryocooler technology continues to advance as mass, power input, vibration levels and cold tip temperatures are reduced while increasing expected operating life and reliability. Table 16 summarizes the performance parameters of some examples of different types of cryogenic refrigerators [Rogatto, 1993].

Table 16. Types of Cryogenic Refrigerators

Type	Manufacturer	Temp (K)	Heat Lift (W)	Power In (W)	Mass (kg)	Specific Power (W/W)	Specific Mass (kg/W)	Lifetime
Stirling Cycle Cooler	TRW (Space Cooler)	65	0.25	14	1.145	56	4.58	10 yr
Brayton Cycle Cyrocooler	Creare, Inc	65	5	200	50	40	10	10 yr
Vuilleumier Cycle Cyrocooler	Hughes Aircraft Corp.	75	12	2700		225		20K hr
Gifford-McMahon Cryocooler	Centre of Advance Technology, Indore India	30	2.6					
Joule-Thomson Cryocooler	MMR Technologies	70	13.6					
Sorption Cryocooler	Jet Propulsion Laboratory	140	2	160		80		
Pulse-Tube Cryocooler	The Cryogenic Laboratory, Beijing, China	77	2.5	188	40.4	75.2	16.16	
Adiabatic Demagnetization Cryocooler	The Univeristy of California, Berkeley	0.1						38 hr

Figure 22 [NASA-JPL, 2006] shows the cyrocooler used on NASA's Atmospheric Infrared Sounder (AIRS). The pulse tube cryocooler is a variation of the Stirling cycle refrigerator. AIRS was the first NASA instrument to use pulse tube coolers. The AIRS focal plane cryocooler, developed under contract with Northrop Grumman, is designed for low vibration, long life, and focal plane operation near 58 K.

Figure 22. Sterling Cryocooler

4.2.5 Displays

Display performance requirements are primarily determined by the characteristics of a human operator and the visual task to which the operator has been assigned. The environment seriously affects the observer's abilities to do even simple tasks. Designers often make errors when they provide excellent displays that require too much time to scan visually. Trade-offs are very important, since the display size may determine the overall utility of an otherwise good sensor system [Rogatto, 1993]. This section briefly describes display technologies, with an emphasis on military applications.

4.2.5.1 Cathode-Ray Tubes

Cathode-ray Tubes (CRTs) represent a mature technology of high reliability in widespread use for black and white or color. The miniature CRT has been and remains the image source of choice for helmet display applications, especially if the image source is also located on the helmet. The cathodoluminescent and faceplate materials used in CTRs can still be improved to obtain desired resolution, luminance, and contrast goals. The small gun apertures and demanding CRT drive conditions associated with high-resolution and high-luminance performance often demand cathode current load levels of 5 to 10 A/cm2. This is well above the 2-A limit that permits reasonable cathode life to be accommodated by conventional oxide cathodes [Rogatto, 1993].

4.2.5.2 Plasma Panels

Plasma panels are transparent panels often containing large arrays of discharge electrodes, usually in a common gas cavity. Both ac and dc versions exist. Plasma display technology is being developed in many sizes and for many applications. For large graphic displays it is the only technology seriously challenging the CTR. Gas discharge tube displays in the form of banks of neon or argon indicator lamps have ling been used. The main problem in terms of their large-scale use has been associated with the fabrication, wiring, and driving of such lamps. Plasma panels are a logical outgrowth to achieve the functions of large arrays of lamps without the conventional difficulties. Plasma panels can be divided into tow basic forms: the ac type, typified by the early Owens-Illinois Digivue® panel and the dc type represented by the early Burroughs Self Scan® panel [Rogatto, 1993].

4.2.5.3 Electroluminescent Panels

Electroluminescent (EL) displays consist of an EL powder or evaporated film between the two electrodes, one of which is transparent. EL displays can be made in may colors. However, most displays are of a single color, usually green or orange because of the higher efficiency achieved with copper-activated and manganese-activated materials. When a potential is applied across the EL material, visible light is emitted. The potential may be ac or dc, depending on the specific structure, but the EL displays usually operate in the ac mode. The resolution or pattern is defined by the electrodes. Luminance is typically 5 to 30 fL, although luminance in the thousands of foot-lamberts was achieved and demonstrated in 1974 [Rogatto, 1993].

4.2.5.4 Liquid Crystals

A thin, clear layer of a cholesteric material placed between transparent electrically conducting covers becomes turbulent when excited by an electric field and scatters ambient light in a manner that yields an apparent brightness related to the applied filed. When an aggregate of such cells forms a two-dimensional array, a digitally addressed display results. These displays can be small light, and relatively inexpensive. The driving circuitry for large arrays is the more costly part, not the liquid crystalline materials, although the cost of microelectronics makes the circuitry rather inexpensive [Rogatto, 1993].

4.2.5.5 Light Emitting Diodes

Light Emitting Diodes (LED) displays are a mature technology for small-scale displays such as those in pocket calculators, small-area indicators, and related applications. Their utility for larger area or ambient brightness applications depends on improved luminous efficiency, lower power dissipation in driving circuits, and costs to challenge other technologies [Rogatto, 1993].

4.2.5.6 Projection Displays

High-luminosity CTRs, including storage tubes such as the Tonotron, liquid-crystal-controlled reflectors, and light values of the oil-film type, are available and useful for various different levels of projected image brightness and size. The projection CTRs fill the needs of small-screen systems. The liquid crystal projection units are relatively small, light, and inexpensive, making them desirable for use in small meetings. The oil-film systems fill the need for small-to-large theater screen displays in black and white or color. A typical devise is the Eidophor. Projection CRT displays are finding increasing application in displays for tactical systems in sizes from 3 to 6 feet on a side. Current tubes, with typical f/0.9 optics, can develop 200 to 300 lm output after optical surface losses. Resolution of 1000 TV lines have been achieved on 5-inch projection CTRs. New longer life and more efficient phosphors are necessary to expand the application of projection CRTs . Oil-film light values are useful for a wide variety of command and control display applications of the fixed-site type. Devices can typically provide 525-line TV images with light outputs of 5000 lm. They are in general large, complex and expensive systems. Small sealed-off light valves are available, but the light output and resolution are limited by light source and cooling. The more recent versions of smaller projection displays utilize projection lamps, mirrors, and LCD elements to switch the various pixels in color and/or black and white. Because the power comes from large projection bulbs, the image size and brightness fill a large number of projection needs for moderate-sized, moderate-resolution, lightweight image projectors [Rogatto, 1993].

4.3 System of Systems

In the vast majority of IR sensor applications, the IR sensor is part of a larger system. Whether integrated into a weapon system, or with multiple sensors, there are significant system engineering challenges in the design of the IR system. Networked sensors provide situational awareness and operational synchronization, and results in added emphasis on integrating imaging sensors and related image processing applications, specifically to address the need to reduce manpower costs by having a computer monitor the imagery and alert the operator when a predetermined event occurs [Ropson, 2005].

Typically decisions will be made based upon the output of multiple sensors, as opposed to a single one. This capability is enabled by automated target recognition (ATR), which is used to determine the area from each sensor that should be examined, as well as the fusion of various sensor outputs to support a threat decision and develop an integrated picture of the battlespace. The large amount of information from the multiple sensors requires an enormous bandwidth to transmit. A solution is using lasercom, optical wavelengths instead of the traditional microwave technology. Laser detection and ranging (LADAR) and passive sensors that use additional phenomenology, such as Multispectral, hyperspectral, and polarization, can be used to identify targets at long range under cover. Though the use of high-energy laser weapons, effects can be brought to the target at the speed of light [Silver, 2005(2)]. Algorithms will be the key differentiator in the future, as computational complexity becomes less of an issue. As features become more distinguishable with higher fidelity sensors, classifiers that have the ability to work with multi-mode distributions of features and can learn on the fly from either internal data sources or new sources will be required. Additionally, these classifiers will need the ability to identify new target classes as they are encountered. Optimization of man-in-the-loop interaction with machines that enables the machines to learn based on human feedback will be required. Fusion techniques will be required that sort through terabytes of imagery and other sensor data to automate cueing or identify objects of interest. [Coit, 2005].

CHAPTER V
MODELING OF INFRARED SYSTEMS

In this chapter, two IR system performance measures are presented. The derivations of these equations are omitted in order to focus on the application and analysis. Most texts referenced in this report include detailed derivations for the inquisitive reader, or as the next step to comprehension. An example analysis is presented along with a parametric approach to system design.

5.1 Noise Equivalent Temperature Difference

Noise Equivalent Temperature Difference (NET, NEΔT, or NETD) is the sensitivity of the thermal system. It is the temperature difference, referenced to 300 K, between a large target and its background, which is required to produce a peak signal to rms noise of one particular point in the signal processing chain. A smaller NEΔT results in a more sensitive system, able to detect and discrimnate between a smaller temperature difference between the target and background. The equation for NEΔT is given as:

$$NE\Delta T = \frac{(\Delta f_n)^{1/2} 4(f/\#)^2}{\pi \tau_0 \tau_A A_d^{1/2} N_s^{1/2} \int \frac{\partial L_\lambda}{\partial T} D_\lambda^* d\lambda}$$ [Dudzik, 1994]

where

$L\lambda$ = spectral radiance (W cm^{-2} sr^{-1} μm^{-1})
$f/\#$ = system effective f/#
τ_0 = optics transmission
τ_A = Atmospheric transmission over the laboratory path used to make the measurement
A_d = detector area (cm^2)
N_s = number of detectors in series
$\Delta\lambda$ = spectral band (μm)
$\partial L_\lambda / \partial T$ = derivative with respect to temperature of the spectral radiance
D^*_λ = spectral detectivity (cm Hz$^{1/2}$ W^{-1})
Δf_n = electronic noise bandpass
NET is commonly referenced to the bandwidth

$$\Delta f_n = \frac{\pi}{2} \Delta f_e = \frac{\pi}{4\tau_D}$$

where

$$\tau_D = \frac{n_p \Delta x \Delta y \eta_{scan}}{\alpha \beta F_R \eta_{ovsc}}$$

and

τ_D = detector dwell time, the time it takes one detector element to scan a point in object space
n_p = number of detectors in parallel
Δx = angular subtense of the detector in the scan direction in milliradians
Δy = angular subtense of the detector in the orthroscan direction in milliradians
η_{scan} = scan efficiency
α = horizontal system field of view in millirandians
β = vertical system field of view in millirandians
F_R = frame rate
η_{ovsc} = overscan ratio = $\Delta y/\Delta y_{sample}$

where

$$\Delta y_{sample} = \frac{\beta}{n_p \times N_{\text{int}\,erlace}}$$

and $N_{interlace}$ is the number of fields per frame.

5.2 Minimum Detectable Temperature Difference

The Minimum Detectable Temperature Difference (MDT or MDTD) is a laboratory measure of a thermal system that, unlike NEΔT, includes the human operator. It relates directly to the noise-limited detection performance of the system and is used to predict detection. The equation for NDT is given as [Dudzik, 1994]:

$$MDT = \frac{NET \times SNR_{T1}}{A_T \int H_T^2 H_D^2 d^2 f} \left[\frac{\Delta y v}{\eta_{ovsc} F_R t_E \Delta f_n} \right]^{1/2} \times$$

$$\left[\int_{-\infty}^{\infty} \int_{0}^{\infty} S(f_x) H_{elect}^2(f_x) H_{display}^2(f_x, f_y) H_{eye}^2(f_x, f_y) H_T^2(f_x, f_y) H_D^2(f_x, f_y) \partial f_x \partial f_y \right]$$

where

A_T = target area (mrad^2)
SNR_{T1} = threshold SNR for the MDT target (empirically 2.25)
H_T = Fourier transform of the target (a circle or square)

H_D = total devise and eye MTF
$S(f_t)$ = normalized noise power spectrum [$S(f_t)=1$ at f_0]
f_0 = measuring frequency at which $S(f_t)$ is normalized
$H_{elect}(f_t)$ = electronics transfer function = $\{1/[1+(f_t/f_0)^2]\}^{1/2}$
$H_{display}$ = display MTF
H_{eye} = eye MTF

5.3 Detection Analysis

The fundamental mechanism of target acquisition is pure detection: the perception of an object against a locally uniform background. This section describes one approach for calculating the probability of pure detection of a target at a given range. The procedure is broken down into four steps. The methodology uses the equations of NEΔT and MDT above. The example here is taken from *The Infrared and Electro-Optical Systems Handbook, Volume 4 Electro-Optical Systems Design, Analysis, and Testing* [Dudzik, 1994] and models a tube-launched, optically tracked, wire-guided (TOW) infrared targeting system. The system characteristics and performance parameters are given in Table 17.

Table 17. Tow System Parameters

System	
Horizontal FOV	2.2 deg
Vertical FOV	1.1 deg
Frame Rate	30 frames/sec
Interlace	2 fields/frame
Scan Efficiency	0.75
System Magnification	12
Spectral Band	7.7-11.75 μm
Optics	
Effective Focal Length	12.0 in.
Effective Aperture Diameter	4.5 in.
f/#	2.667
Average Optical Transmittance	0.57
Diffraction Wavelength	10.0 μm
Blur Spot Size	0.007 $mrad^2$
Detector	
Detector $IFOV_x$	0.133 mrad
Detector $IFOV_y$	0.200 mrad
Detectors in Parallel	60
Detectors in Series	1
Limited System Noise	Detector
Peak D*	5.1 X 10^{10} cm $Hz^{1/2}$ W^{-1}
Display	
Display Type	EO mux LED array
Average Luminance	10.0 mL
LED $Subtense_x$	0.0625 mrad
LED $Subtense_y$	0.3130 mrad

Initially, determine the target's inherent ΔT. Calculate the target area and the target's projected angular subtense at rang R. Using knowledge of the atmospheric transmission, calculate the apparent ΔT of the target at range R. The physical size of the M60 target front is 3.6 m wide by 3.2 m height, resulting in a total area of 11.52 m^2. At range of 6 km, the projected angular subtense is .32 $x10^{-6}$ sr.

$$A_s = \frac{A_0}{R^2} = \frac{11.52m^2}{6km} = 0.32\times10^{-6}$$

The performance of the imager will be compared in two atmospheres. The first is a good atmosphere corresponding to a visible range of 23 km, relative humidity of 50% and air temperature of 15°C. These conditions are termed "U.S. Standard, Spring-Summer" atmosphere in the LOWTRAN 7 (Philips Laboratory) atmospheric model. The second is a poor atmosphere with 5 km visibility range, 75% relative humidity, and an air temperature of 27°C. These conditions describe the "Tropical Spring-Summer" atmosphere. In this example the inherent ΔT of the M60 target is given as 1.25°C. The apparent target ΔT is a function of range due to the attenuation of the signal by the atmosphere. The total transmission integrated over the spectral band of the TOW system is determined using LOWTRAN 7. The data is estimated and reproduced in Figure 23, plotted versus the range.

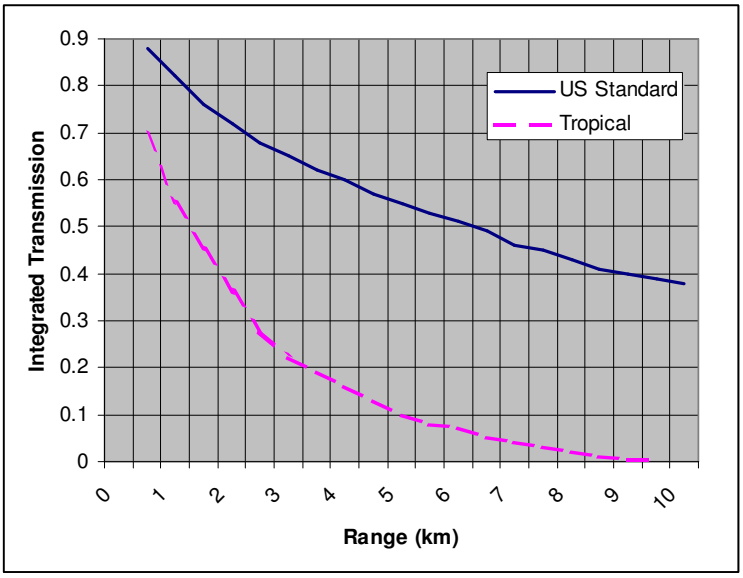

Figure 23. Total Integration Transmission Versus Range

This is used to determine the apparent temperature at a particular range. At a range of 6 km the atmospheric transmission is 51% and 7.5% found from Figure 23, resulting in apparent ΔT of 0.64°C and 0.093°C for the good and poor conditions, respectively.

$$\Delta T_{apparent} = \Delta T_{Inherent} \times \tau_A = 1.25^0 C \times 0.51 = 0.64^0 C \text{ (U.S. Standard)}$$

$$1.25^0 C \times 0.075 = 0.093^0 C \text{ (Tropical)}$$

Next, calculate the system MDT. NEΔT is one of the parameters in MDT and is calculated using the equation above in Section 5.1. Using the TOW system parameters, The NEΔT is calculated to be 0.17°C. The calculations are shown below.

$$\Delta y_{sample} = \frac{\beta}{n_p \times N_{\text{int}erlace}} = \frac{19.198}{60 \times 2} = 0.159984 \text{ mrad}$$

$$\eta_{ovsc} = \frac{\Delta y}{\Delta y_{sample}} = \frac{0.200}{0.159984} = 1.250$$

$$\tau_D = \frac{n_p \Delta x \Delta y \eta_{scan}}{\alpha \beta F_R \eta_{ovsc}} = \frac{60 \times 0.133 \times 0.2 \times 0.75}{38.396 \times 19.198 \times 30 \times 1.250} = 4.33 \times 10^{-5} \text{ sec}$$

$$\Delta f_n = \frac{\pi}{4\tau_D} = \frac{3.141}{4 \times \left(4.33 \times 10^{-5}\right)} = 1.8139 \times 10^4$$

$$NE\Delta T = \frac{(\Delta f_n)^{1/2} 4 (f/\#)^2}{\pi \tau_0 \tau_A A_d^{1/2} N_s^{1/2} \int \frac{\partial L_\lambda}{\partial T} D_\lambda^* d\lambda}$$

$$= \frac{\left(1.8139 \times 10^4\right)^{1/2} \times 4 \times 2.667^2}{3.141 \times 0.57 \times 0.51 \times (102.6)^{1/2} \times 1^{1/2} \times \left(1.18 \times 10^{-8}\right) \times \left(5.1 \times 10^{10}\right) \times (11.75 - 7.7)} = 0.17^0 C$$

The NEΔT is used to calculate MDT using the equation in Section 5.2. The resulting MDT is then normally plotted against the inverse target size ($mrad^{-1}$). Knowing the target subtense and having calculated the system MDT, the threshold temperature difference required to just detect the target is read off the MDT graph (not shown here). In this example, the threshold temperature difference is determined to be 0.058°C. The calculations and graph is omitted, the reason for which will become apparent.

Now, knowing both the target apparent temperature difference and the threshold temperature difference, the SNR can be calculated using

$$SNR = \frac{apparent\Delta T}{threshold\Delta T} \times SNR_{T1} = \frac{0.093}{0.058} \times 2.25 = 3.61$$

The probably of detection is then determined from the empirical relationship between SNR_D versus P_D. For a SNR of 3.61 and Tropical conditions, the probability of pure detection is 77%.

5.4 IR System Analysis

The objective in this approach is to increase the probability of pure detection. It is obvious that a larger SNR increases the probability of detection. A larger MDT increases the threashold temperature difference, which is inversely proportional to SNR. A smaller MDT is desired to increase SNR and P_D. The NEΔT is directly related to MDT, so it follows that decreasing NEΔT will increase PΔ. The characteristics and performance parameters of the IR system are within the calculations of NEΔT. Therefore, if the goal is to design a system that improves the probability of detection, we can analysis NEΔT by varying system parameters in order to minimize NEΔT, knowing it will have the desired outcome. The following figures show the impact to NEΔT of varying four system parameters: Frame rate, Detectivity, Scan Efficiency, and Optics transmission.

Frame rate affects the transfer rate of the image to the detectors (Figure 24). It is inversely proportional to the detector dwell time, the time it take one detector element to scan a point in space. This is part of the mechanical design of the detector component. As the graph shows, slowing down the frame rate, creating a longer dwell time gives a reduced NEΔT.

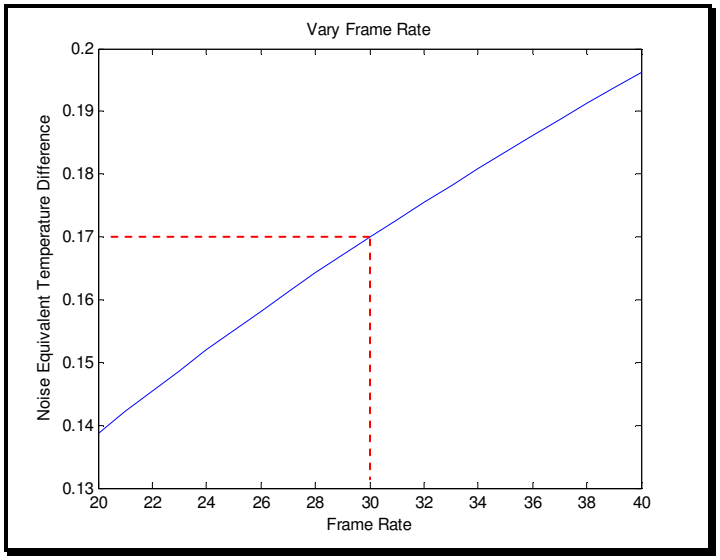

Figure 24. Frame Rate

Detectivity (D*), as described in Section 3.5.13, is the reciprocal of Noise Equivalent Power (DEP) normalized for detector area and bandwidth. NEP is the signal level that produces a signal-to-noise ratio of 1. A detector of higher D* requires a less powerful incident signal to discriminate it from the noise in the signal. As D* increases, NEΔT decrease and gives a higher P_D (Figure 25).

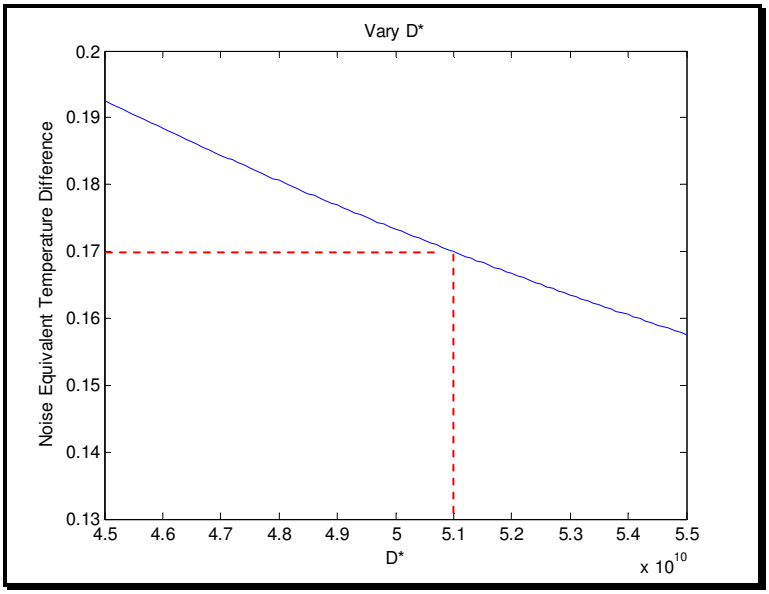

Figure 25. Detectivity

Scan Efficiency is the ratio of active scan time to one field time. As the scanning mirror oscillates, it is inactive during the time in which it changes direction outside the FOV. There is a reduction in time that the mirror is reflecting photons to the detector. An improvement in scan efficiency reduces NEΔT with an increase in P_D (Figure 26). The scan efficiency is affected by the mechanical design of the optical components. As described in Section 3.1.6, Kirchoff's Law showed that radiant energy is reflected, transmitted, or absorbed.

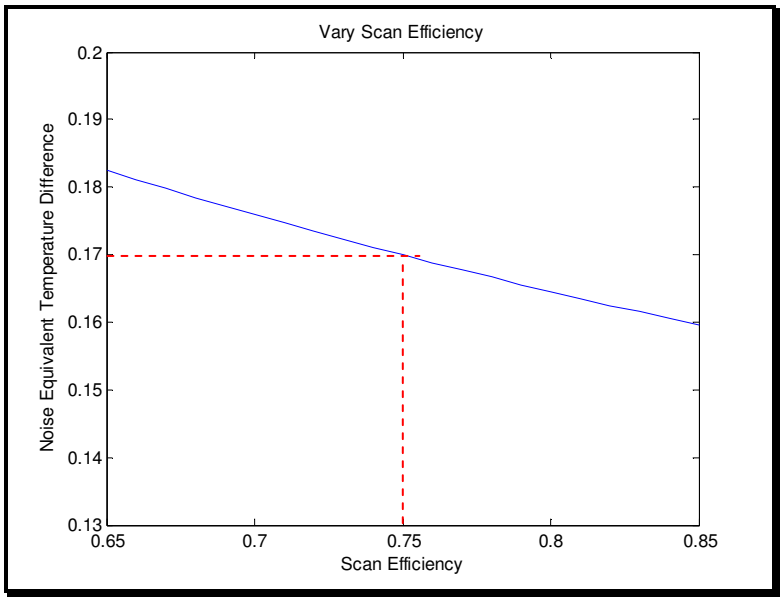

Figure 26. Scan Efficiency

Optics transmission is the ratio of energy that is transmitted through the optical devises. The more energy transmitted, and not absorbed or reflected, increases the energy incident on the detectors decreases the NEΔT, again increasing P_D. The optical materials described in Section 4.2.1.3 affect the optical transmission. The absorption coefficient is a measure related to the materials and chemicals used to fabricate and coat the lenses.

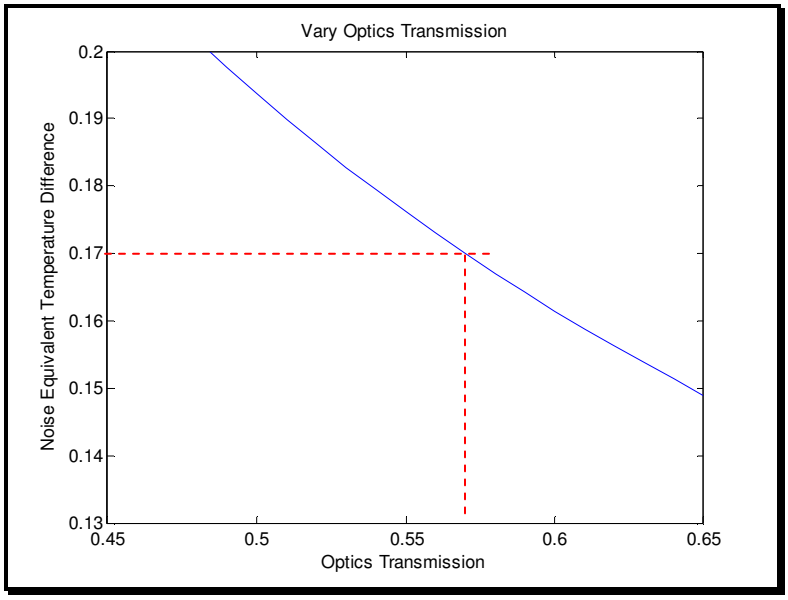

Figure 27. Optics Transmission

In this analysis, it is shown that changes to each of these characteristics of the system have the potential to improve PΔ. However, each improvement requires a different engineering discipline and a different technology. It requires a multi-disciplined, systems engineering approach to determine the best solution. Additionally, with each of these variations, there are other considerations. The system may be constrained for weight, volume, or power consumption. Cost of the system is another factor. Though it may be obvious from the graphs that an incremental increase in D* has better result than the other parameters, the cost of achieving the desired D* may not be feasible, or the technology may not exist. Various design tradeoffs are required to arrive at the optimal solution.

There are several other IR system performance measures that can be used to predict the required outcome. This is a simple example intended to demonstrate an approach, and to emphasize the need for systems engineering and tradeoff analysis.

CHAPTER VI
CURRENT CAPABILITES

This chapter describes just a few systems boasting the latest capabilities in EO and IR sensors. All descriptions come from open source internet material, brochures, and data sheets to avoid classified or company proprietary information. These systems have been proven on the battlefields of Iraq and Kuwait, often fast-tracked through the development and production phases to meet the war fighters' needs.

6.1 AN/ASQ-228 Advanced Targeting Forward Looking Infrared (ATFLIR)

Raytheon's ATFLIR pod is a third generation targeting system, replacing the existing electro-optic sensor suite by combining separate midwave infrared navigation FLIR and targeting FLIR pods into one integrated unit. The single pod also integrates a laser range finder and target designator. Its target detection range is four times better than previous systems and its laser designation function is effective up to 50,000 feet at a slant range of over 30 miles. The electro-optical imagery boasts 3 to 5 times greater clarity than other similar pods in production, using a 640 X 480 InSb focal plane array. It has 360 degree roll drive, with continuous automatic boresight alignment, which guarantees continuous target coverage and first-pass kill capability. The built in diagnostics and solid-state, fiber optic gyros enhance the pod's reliability [O'Melveny, 2005]. The ATFLIR is shown in Figure 28 [O'Melveny, 2005], integrated by Boeing on their F/A-18E Super Hornet.

Figure 28. ATFLIR

6.2 AN/AAS-52 Multi-Spectral Targeting System (MTS)

The MTS multi-sensor payload integrates infrared and CCDTV sensors, laser rangefinder, designator, and illuminator with optional additional of a laser spot tracker. The MTS provides high rate of stabilization on six axes and flexible operating modes including line-of-sight targeting for laser designation, sensor fusion and automatic target tracking, using centroid, area and feature tracks. The MTS-B , shown in Figure 29 [Defense Update, 2005], is designed for the Predator-B Unmanned Ariel Vehicle (UAV) hunter-killer missions.

Figure 29. MTS

This version uses a 20-inch ball with visible and IR imagers, to provide long range surveillance from high altitude, including a 2048 X 2048 pixel focal plane array which enables a footprint of 200 X 48 meters from 25,000 feet. The footprint of the standard MTS-A, designed for the original Predator model is 50 X 10 meters at 10,00 feet. This capability dramatically improves the resolution and coverage of the sensor. Utilizing existing digital zoom, up to x4 factor, the extended range sensor can quadruple the area coverage capacity of the sensor, when adequate bandwidth is provided by the system. The MTS performs intelligence gathering plus target acquisition and engagement tasks by tracking, range finding, and laser designation for on-board or remotely fired laser guided weapons such as the Hellfire missile [Defense Update, 2005]. The MTS-A has also been modified for use on the Navy's H-60 helicopter.

6.3 AN/PAS-13B Thermal Weapon Sight

The AN/PAS-13B Thermal Weapon Sight is a compact, lightweight, battery powered, infrared sight system developed by Raytheon for the US Army is shown in Figure 30. It has a dual field of view, which allows it to be used as a hand-held telescope or weapon-mounted sight. The "Medium" version has a wide field of view (WFOV) of 18^{o} azimuth and 10.8^{o} in elevation with 1.66x magnification. The narrow field of view (NFOV) is 6^{o} azimuth and 3.6^{o} in elevation with 5.0x magnification. The FOVs for Heavy version, for higher caliber machine guns, is about half that of the Medium version, resulting in twice the magnification.

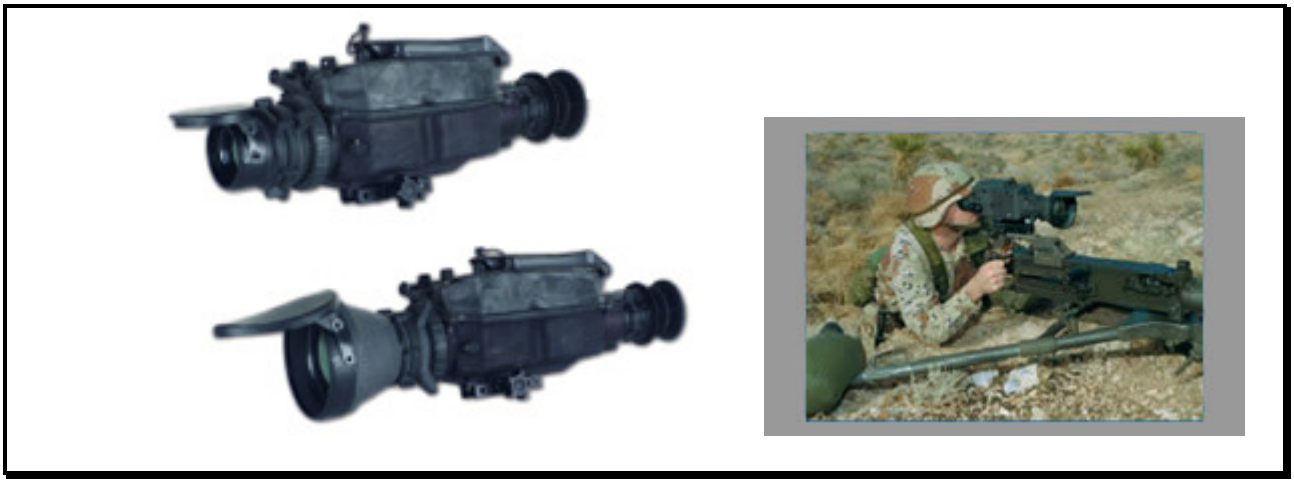

Figure 30. Thermal Weapon System

The high-sensitivity mercury cadmium telluride (HgCdTe) focal plane array provides long-rang target recognition with a relatively small scope, and includes a thumbnail-sized thermoelectric cooler. The scanning focal plane array is 40 X 16 (640 pixels) with capability in the 3 to 5 µm IR spectrum. The Heavy model NFOV achieves human detection at 2.8 kilometers and vehicle detection at 6.9 kilometers.

6.4 AN/AAQ-28(V) LITENING AT

The fourth generation version of LITENING, built by Northrop Grumman, features the 1024 x 1024 pixels FLIR sensor for improved target detection and recognition ranges under day/night conditions; new sensors for improved target identification; and other advanced target recognition and identification features. Other product improvements include a new 1k charge-coupled device sensor, which provides improved target detection and recognition ranges under daylight conditions. The LITENING AT is shown in Figure 31.

Figure 31. LITENING AT

The LITENING AT system is a self-contained, multi-sensor laser target-designating and navigation system that enables aircrews to detect, acquire, track and identify ground targets for highly accurate delivery of both conventional and precision-guided weapons. It is currently deployed on AV-8B, A-10, B-52, F-15E, F-16 and F/A-18 aircraft. Since the introduction of LITENING in 1999, the system has undergone numerous major upgrades to ensure continued combat relevance in an ever-changing battlespace, with the fourth generation version the next step in that evolution.

6.5 NICMOS –Hubble Space Telescope

Aboard the Hubble Space Telescope is the Near Infrared Camera and Multi-Object Spectrometer (NICMOS). NICMOS, shown in Figure 32 [Hubblesite, 2006], was built by Ball Aerospace and installed in the Hubble Space Telescope during the 1997 Second Servicing Mission. The instrument's three detectors, each with different fields of view, are designed to see objects in the near-infrared wavelengths. By studying objects and phenomena in this spectral region, astronomers probe our universe's past, present, and future, learn how galaxies, stars, and planetary systems form, and reveal a great deal about our universe's basic nature. NICMOS must operate at very cold temperatures, below –321^{o}F, or 77 K. The instrument's detectors used to be cooled inside a cryogenic dewar. When NICMOS was installed in 1997, the dewar contained a 230-pound block of nitrogen ice. The dewar, which successfully cooled the detectors for about two years, ran out of coolant prematurely. NICMOS was rechilled during Servicing Mission 3B with a cryocooler, a machine that operates much like a household refrigerator [Hubblesite, 2006].

Figure 32. NICMOS

CHAPTER VII
SUMMARY

What a journey! The limited scope of this report does not allow for a comprehensive view of EO and IR technology. It takes eight volumes to cover this topic in the *IR/EO Systems Handbook*. This report could only include a very basic presentation of the theories that define the infrared sensor in Chapter III. A brief view of just a few materials used for the major components was covered in Chapter IV. Along with target detection, addressed in Chapter V, there is target orientation, recognition, identification, and classification. There are numerous commercial, government, and military applications that were not shown as examples in Chapter VII.

Admittedly, there are several areas omitted, but require additional attention and learning. The complex sensor systems require digital and image signal processing for automated target detection and automatic target recognition (ATD/ATR). This report focuses almost exclusively on passive OE, with very little about active EO systems. Another area is networked sensors that require data fusion algorithms and high-speed processors as part of an integrated system. An emerging capability is autonomous sensor networks, miniaturized sensors of various types including IR, spread across an area that automatically form a network, establish communication protocols and transmit data to a central station.

However, the reader should now have a better understanding of how the sensor works, the basic engineering principles, and the importance of systems engineering in the design of the system. The reader can extend the learning process through the texts and periodical referenced in this report.

Now you know what you don't know about IR sensors.

REFERENCES

1. [Jha, 2000] Infrared Technology: Applications to Electro-Optics, Photonic Devices and Sensors; 2000, A. R. Jha

2. [Dereniak, 1984] Optical Radiation Detectors; 1984, Eustace L. Dereniak and Devon G. Crowe.

3. [Lloyd, 1975] Thermal Imaging Systems; 1975, Michael J. Lloyd.

4. [Rogatto, 1993] The Infrared and Electro-Optical Systems Handbook, Volume 3 Electro-Optical Components; 1993, William D. Rogatto, Editor.

5. [Lawson, 1959] "Preparation and properties of HgTe and mixed crystals of HgTe-CdTe", Journal of Physics and Chemistry of Solids, Vol 9, pp. 325-329; 1959.

6. [Groves, 2002] Thermal Imagers and Camouflage; Dr. James M.C. Groves, 2002. Website: http://www.btinternet.com/~jmcgroves/thrmalim.htm

7. [Dudzik, 1993] The Infrared and Electro-Optical Systems Handbook, Volume 4 Electro-Optical Systems Design, Analysis, and Testing; 1993, Michael C. Dudzik, Editor.

8. [Ullman, 1996] Shock and Awe: Achieving Rapid Dominance; 1996; Harlan K. Ullman, James P. Wade, et al.

9. [Varsarno, 2005] Algorithms for tracking point targets in infrared sequences; L. Varsarno, V. Adler, and S.R. Rotman; Proceedings of the SPIE, Vol 5987, Oct. 11, 2005.

10. [Norton, 2002] HgCdTe Infrared Detectors; P. Norton; Opto-Electronics Review vol. 10(3), 159–174 (2002).

11. [NASA, 2001] Infrared Waves – The Electromagnetic Spectrum Website: http://imagers.gsfc.nasa.gov/ems/infrared.html

12. [Wikipedia, 2006] Wikipedia, the free encyclopedia. Website: http://en.wikipedia.org/wiki/

13. [Works, 2006] How Stuff Works "How Night Vision Works". Website: http://science.howstuffworks.com/nightvision1.htm

14. [Marquis, 2003] "Fundamentals of Thermal Imaging Systems"; 2003, Author: Mike Marquis; Raytheon (Presentation Slides for FLIR101, May 2006).

15. [O'Melveny, 2005] Military.Com "THE SMART POD: Infrared Pods Reach Mass Production"; 2005 Sean O'Melveny; Websit: http://www.military.com/soldiertech/0,14632,Soldiertech_ATFLIR,,00.html

16. [Defense Update, 2005] Defense Update "Multi-Spectral Targeting System (MTS) AN/AAS-52" ; 2005; Website: http://www.defense-update.com/products/m/MTS.htm

17. [Defense Update, 2006] Defense Updated "Tank Urban Surviblity Kit"; 2006; Website: http://www.defense-update.com/products/t/tusk.htm

18. [Shaw, 2003] Spectral Imaging for Remote Sensing; Gary A. Shaw and Hsiao-hua K. Burke; Lincoln Laboratory Journal, Vol 14 (1), 2003.

19. [Johnson, 1928] "Thermal Agitation of Electricity in Conductors", J.B. Johnson; Physics Review, Vol. 32, 1928.

20. [Thorlabs, 2006] "IR Optics"; Thorlabs, Inc., 2006; Website: http://www.thorlabs.com/Navigation.cfm?Guide_ID=132&Visual_ID=1607

21. [Northrop, 2005] "M2105 Series PbS Focal Plane Arrays"; Northrop Grumman, Electronic System, 2005; Website: http://www.es.northropgrumman.com/es/eos/ir_products.htm

22. [ORNL, 2003] "Energy Efficiency and Renewable Energy Program"; Oak Ridge National Laboratory, one of the Department of Energy's national research and development facilities, managed by UT-Battelle, LLC, 2003; Website: http://www.ornl.gov/sci/eere/industry/sensors/lowpower.htm

23. [NASA-JPL, 2006] "AIRS Technology Subsystems, Cryocooler Assembly"; NASA Jet Propulsion Laboratory, California Institute of Technology, 2006; Website: http://www-airs.jpl.nasa.gov/Technology/Subsystems/CryoCooler/

24. [Silver, 2005(1)] "Part 1 of 2 Electro-optical Technology Features"; Alan Silver; Technology Today, Raytheon, Issue 1, 2005.

25. [Johnson, 2005] "Enabling Technologies"; Scott Johnson; Technology Today, Raytheon, Issue 1, 2005. Website: http://home.ray.com/rayeng/news/technology_today/v3_i4/feature_7.html

26. [Silver, 2005(2)] "Part 2 of 2 Electro-optical Technology Features"; Alan Silver; Technology Today, Raytheon, Issue 2, 2005.

27. [Ropson, 2005] "Raytheon's Role in Homeland Security"; Steven Ropson; Technology Today, Raytheon, Issue 2, 2005.

28. [Coit, 2005] "Autonomous Target Recognition"; Al Coit; Technology Today, Raytheon, Issue 2, 2005.

29. [Hubblesite, 2006] "HST Instruments Defined"; Hubblesite, 2006; Webstie: http://hubblesite.org/the_telescope/nuts_.and._bolts/instruments/nicmos/